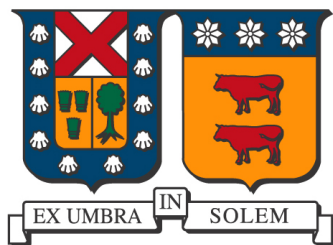


DEPARTAMENTO DE FÍSICA
UNIVERSIDAD TÉCNICA FEDERICO SANTA MARIA



PhD Thesis

Modern detectors to study the Standard Model and beyond

Author:
Gerardo Vásquez Arenas

Supervisor:
Professor Sergey Kuleshov

Valparaíso, 2017

Abstract

The increased necessity of experimental proof of physics beyond Standard Model (SM) and Dark Matter theories leads us to develop new detectors for high energy experiments, such as ATLAS with its upgrade (New Small Wheel project in particular) for the luminosity increase at LHC, and a new experiment on SPS facilities at CERN called NA64 to search for Dark Matter on invisible (visible) decays of dark photons.

For these two experiments, detectors from the Physics department of the Technical University Federico Santa Maria in Valparaiso (Chile) have been built **to be part of such enterprise.**

Characterizations and tests have been conducted with the use of particles beam (electrons, pions, muons and gamma rays) from the Experimental Area at CERN.

Contents

1. Introduction	7
1.1. Interaccion of Radiation with Matter	7
1.2. Gas filled detectors	7
1.2.1. Production of Electron-Ion pairs	7
1.2.2. Diffusion and Drift of Charges in Gases	7
1.2.3. Regions of Operation of Gas Filled Detectors	7
1.3. Scintillation detectors	7
1.4. Calorimeters	7
1.4.1. Radiation Length	7
2. Small-strip Thin Gap Chamber	9
2.1. High Luminosity Large Hadron Collider	9
2.2. ATLAS Detector	10
2.2.1. Coordinate system	11
2.2.2. Detector Upgrade	12
2.3. sTGC Description	13
2.3.1. Electric field simulation	14
2.4. Construction process	15
2.5. Gain uniformity measurements	18
2.5.1. Setup	19
2.5.2. Results	21
2.6. Stability under high rate	22
2.7. Spatial Resolution	27
2.7.1. Analysis Model	28
2.8. Pad efficiency	32
2.9. Summary	35
3. High count rate γ-ray spectroscopy in GIF++	37
3.1. Introduction	37
3.2. Counter Limit	37
3.3. High Radiation Source	37
3.4. Data Analisys	37
3.4.1. Multiple hits	37
3.4.2. Wavelets	37

3.4.3. Peak identification	38
3.5. Results	38
3.5.1. Spectrum	38
3.5.2. Gamma Flux Rates	38
4. Synchrotron radiation detector for e^- tagging	39
4.1. NA64 experiment	40
4.1.1. Physics Motivation	41
4.1.2. Dark Photon signal	41
4.1.3. Detector	43
4.2. The synchrotron radiation tagging system	44
4.2.1. Cherenkov Radiation	45
4.2.2. Synchrotron Radiation	46
4.2.3. BGO	48
4.2.4. LYSO	49
4.3. Calibration	51
4.4. Time resolution	59
4.5. Hadron rejection	61
4.5.1. BGO hadron suppression	61
4.5.2. Total energy	61
4.5.3. Strips triggered	61
4.6. Experimental Results	68
4.7. Summary	68
5. Conclusion	69
A. Appendix	71
A.1. Mechanical Measurements sTGC Module 0	71
A.2. PMT RT7525 Data Sheet	71
A.3. NA64 Experiment:Data structure	71
A.4. NA64 Experiemnt:DAQ system	71

1. Introduction

In this chapter we present a review of the physics for radiation detectors. The basic features of radiation detectors can be understood once fundamental processes of radiation interaction in matter are considered.

1.1. Interaction of Radiation with Matter

5 pages

1.2. Gas filled detectors

5 pages

1.2.1. Production of Electron-Ion pairs

1.2.2. Diffusion and Drift of Charges in Gases

1.2.3. Regions of Operation of Gas Filled Detectors

1.3. Scintillation detectors

3 pages

1.4. Calorimeters

1.4.1. Radiation Length

The radiation length is the distance over which the radiative emission is the dominant energy loss process and the screening parameter η approaches to 0, the total radiation cross section is that for complete screening except in the case of high frequency emitted photons. This cross section does not depend on the incoming electron energy E_0 . For a complete screening in the Born approximation, the quantity X_0 is introduced as:

$$X_0 = \frac{1}{[4n_A \bar{\Phi}_c \ln \left(\frac{183}{Z^{1/3}} \right)]} \text{[cm]} \quad (1.1)$$

4 pages

2. Small-strip Thin Gap Chamber

The aim of this chapter is to show the characteristics of new detectors to be used as part of the ATLAS experiment upgrade, and how to achieve the requirements of the high luminosity operation. The results of each test to characterize the detector are presented in this chapter.

2.1. High Luminosity Large Hadron Collider

The Large Hadron Collider (LHC), located at the European Organization for Nuclear Research (CERN, derived from *Conseil Européen pour la Recherche Nucléaire*) at the Franco-Swiss border near Geneva is a circular accelerator of 27km circumference of acceleration pipes, constitutes the largest scientific instrument ever designed and built for scientific research. It has been successfully commissioned in March 2010 for proton-proton collision with a 7 GeV center-of-mass energy.

The LHC is pushing the limits of human knowledge, enabling physicists to go beyond the Standard Model (SM): the enigmatic Higgs boson, the mysterious Dark Matter and the world of super symmetry are just three of the long-awaited mysteries that the LHC is working to unveil.

The announcement given by CERN on 4 July 2012 about the discovery of a new boson at 125-126GeV[1, 2], almost certainly the long awaited Higgs particle, is the first fundamental discovery, hopefully the first of a series, that the LHC can deliver.

Such discovery was made possible thanks to the general-purpose detectors ATLAS and CMS, both located at 2 interaction regions, complemented by the specialized detectors ALICE and LHCb.

	Period	Energy \sqrt{s}	Luminosity \mathcal{L}	Integrate \mathcal{L}
Run I	2010-2012	7-8 TeV	$6 \times 10^{33} \text{ cm}^{-2}\text{s}^{-1}$	25 fb^{-1}
LS1	2013-2014	LHC: Go to design energy, nominal luminosity, bunch spacing 25ns		
Phase 0	2015-2018	14 TeV	$1 \times 10^{34} \text{ cm}^{-2}\text{s}^{-1}$	75 fb^{-1} to 100 fb^{-1}
LS2	2019-2020	ATLAS: Upgrade μ spectrometer;NSW,LAr Calorimeter & FTK		
Phase 1	2021-2023	14 TeV	$2 \times 10^{34} \text{ cm}^{-2}\text{s}^{-1}$	$\sim 350 \text{ fb}^{-1}$
LS3	2024-2025	ATLAS: New Inner Tracker and trigger architecture		
Phase 2	2026-2030	14 TeV	$5 \times 10^{34} \text{ cm}^{-2}\text{s}^{-1}$	$\sim 3000 \text{ fb}^{-1}$

Table 2.1: LHC Schedule & upgrades for ATLAS detector.

The LHC baseline programme until 2030 is shown in Table 2.1. After entering into the nominal energy regime of 13 TeV to 14 TeV centro-fo-mass energy in 2015, it is expected that the LHC will reach the design luminosity of $1 \times 10^{34} \text{ cm}^{-2}\text{s}^{-2}$. This peak value should give a total integrated luminosity of about 40 fb^{-1} per year. In the period 2019-2023 the LHC will hopefully further increase to two times the peak luminosity, reaching at the end of 2023 an integrated luminosity of about 350 fb^{-1} .

After the Long Shutdown 3 (LS3) the machine will be in the High Luminosity configuration (HL-LHC). For its successful realization, a number of key novel technologies have to be developed, validated, and integrated, accompanied with upgrades from the general purpose detectors such as ATLAS.

2.2. ATLAS Detector

The ATLAS detector is a general-purpose experiment, designed to explore proton-proton collisions at center of mass up to $\sqrt{s} = 14 \text{ GeV}$ in the Large Hadron Collider (LHC) at the European Laboratory for Particle Physics (CERN). It is aiming to understand the foundations of matter and forces, in particular the nature of mass in a broad physics program. The ATLAS detector was built with the ability to discover the Higgs boson over a wide mass range. It can also perform searches for the production of heavy particles that would indicate physics beyond the Standard Model, such as super symmetric particles, as well as searches for other massive objects.

The ATLAS experiment includes complex detector systems. The central part is a cylindrical Inner Detector, to detect charged particles produced in the collisions, and as such, it is a compact and highly sensitive component. It consists of three different systems of sensors, all immersed in a magnetic field parallel to the beam axis. The **Inner Detector** measures the direction, momentum, and charge of electrically-charged particles produced in each proton-proton collision. The next part is the Calorimeter (red and green on figure 2.1), which measures the energy of a particle when it loses its energy as it passes through the detector. It is usually designed to stop entirely or “absorb” most of the particles coming from a collision, forcing them to deposit all of their energy within the detector. Calorimeters typically consist of layers of “passive” or “absorbing” high-dense material -for example, lead-interleaved with layers of an “active” medium such as scintillator or liquid argon.

Electromagnetic calorimeters measure the energy of electrons and photons as they interact with matter. Hadronic calorimeters sample the energy of hadrons (particles that contain quarks, such as protons and neutrons) as they interact with atomic nuclei. The components of the ATLAS calorimetry system are: the **Liquid Argon (LAr) Calorimeter** and the **Tile Hadronic Calorimeter**.

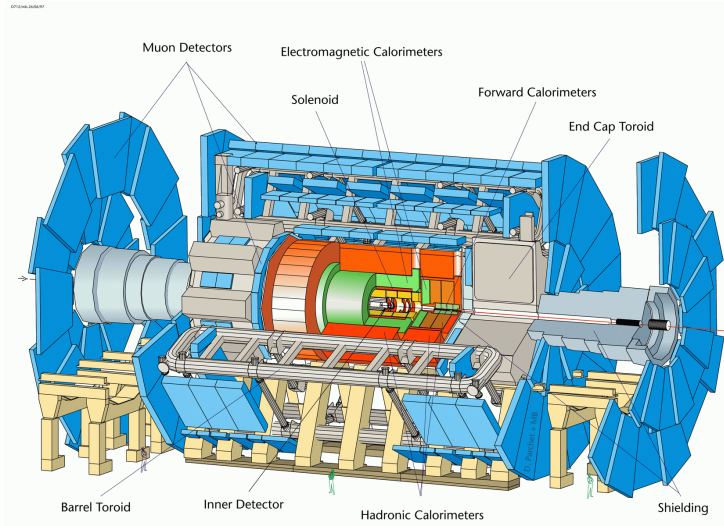


Figure 2.1: ATLAS detector, Muon Spectrometer (in blue)

Calorimeters can stop most known particles except muons and neutrinos. Muons are charged particles that pass through the Inner Detector and Calorimeter interacting only by ionization, they can penetrate through large amount of material without any strong interaction, they have long lifetime, therefore, can be considered as stable particles within the detector's volume, and provide a good tagging for the lepton's decays channels.

To trigger and detect these particles, the ATLAS experiment uses the **Muon Spectrometer**, made up of 4.000 individual muon chambers (different types of gas chambers) which are in charge of identify each one of these muons. It is only possible to measure their momentum with the help of the **Magnet System**, made of three sections; the **Central Solenoid Magnet** with a 2T magnetic field that bends the charged particles for momentum measurement near the interaction points, helping the Inner Tracker system, the **Barrel Toroid** bends the muon particles in the low rapidity region, and the **Endcap Toroid** with a 4T magnetic field that bends the muons in the high rapidity region.

2.2.1. Coordinate system

A common coordinate system is used through ATLAS. The interaction point is defined as the origin of the coordinate system. The z-axis runs along the beam line. The x-y plane is perpendicular to the beam line and is referred to as the transverse momentum, p_T . The positive x-axis points from the interaction point to the center of the LHC ring; the positive y-axis points upward to the surface of the earth. The detector which is located half at positive z-values is referred to as the “A-side”, to the other half the “C-side”. The transverse plane is often described in terms of $r - \phi$ coordinates. The azimuthal angle ϕ is measured from the x-axis, around the beam. The radial dimension, r , measures the distance from the beam line. The polar angle θ is defined as the angle from the positive z-axis. The polar angle is often reported in terms of pseudorapidity, defined as $\eta = -\ln \tan(\theta/2)$. The distances ΔR is defined in $\eta - \phi$ space as $\Delta R = \sqrt{\Delta\eta^2 + \Delta\phi^2}$.

2.2.2. Detector Upgrade

To fulfill the LHC program (in table 2.1), and in order to benefit from the expected high luminosity performance that will be provided by the Phase-I upgraded LHC, the first station of ATLAS muon end-cap system (Small Wheel, SW) will need to be replaced. The **New Small Wheel (NSW)** will have to operate in a high background providing a radiation region (up to 15 kHz/cm^2 of photons, and 75 Hz/cm^2 of neutrons is expected) while reconstructing muon tracks with high precision as well as furnishing information for the Level-1 trigger. These performance criteria are demanding. In particular, the precision reconstruction of tracks for offline analysis requires a spatial resolution of about $100\mu\text{m}$, and the Level-1 trigger track segments have to be reconstructed online with an angular resolution of approximately 1mrad.

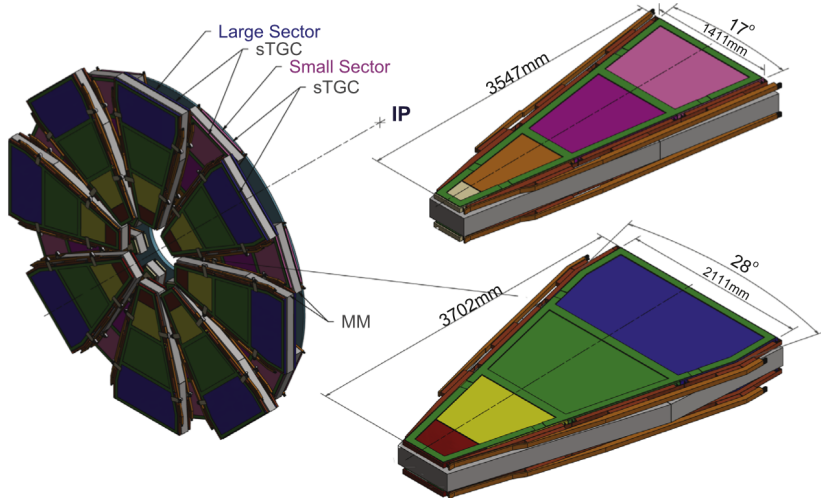


Figure 2.2: New Small Wheel

The NSW will have two chamber technologies, one primarily devoted to the Level-1 trigger function (Small-strip Thin Gap Chambers, sTGC) and the other one dedicated to precision tracking (Micromegas detectors, MM). The sTGC is deployed for triggering given their single bunch crossing identification capability, a fast response and good position resolution.

The MM detectors have exceptional precision tracking capabilities due to their small gap (5mm) and strip pitch (approximately 0.5mm). Such a precision is crucial to maintain the current ATLAS muon momentum resolution in the high background environment of the upgraded LHC. The MM chambers can, at the same time, confirm the existence of track segments found by the muon end-cap middle station (Big Wheels) online. The sTGC has the additional ability to measure offline muon tracks with good precision, so the sTGC-MM chamber technology combination forms a fully redundant detector system for triggering and tracking both for online and offline functions. This detector combination has been designed to be able to provide excellent performance for the eventual High Luminosity LHC upgrade.

2.3. sTGC Description

The small-strip Thin Gap Chamber (a.k.a sTGC) is a multi-wire proportional chamber (MWPC), a detector type with a relatively old technology. Its successful introduction to detector systems in 1968 has earned eGeorges Charpak the Nobel prize in Physics 1992. Those devices have been a major ingredient to detector systems since they can achieve spatial resolution of tenths microns, and have typical time resolution of about 50ns.

The sTGC has been design to exploit these features, working with a cathode-anode pitch smaller than the anode-anode pitch, mostly based on the design of the Thin Gap Chamber[3], with thinner strips as the main improvement from the previous version. The TGC technology has been used since 1988 in the OPAL experiment[4] and is currently part of the muon spectrometer in ATLAS.

This new chamber has the advantage of having a 3.2mm strip-pitch compared with the 6mm from the previous TGC, which explains the *small-strip* prefix.

Chambers with different strips sizes were built and tested under pion beams, and the 3.2mm pitch was chosen as the best option to provide a resolution better than $100\mu\text{m}$ [5]. This change will improve the measurement of charge centroid position by charge interpolation.

To improve the time response, the cathode surface resistivity has been reduced by a factor 10, to reduce charge accumulations on the cathode when chamber operates at high rate, lowering from $1\text{ M}\Omega/\square$ to $100-200\text{k}\Omega/\square$ resistivity on the graphite layer. At the same time, cathode-readout plane (strips or pads) distance was reduced to 0.1mm(1.6mm before) to increase the capacitive coupling by 10, therefore the RC factor keeps unchanged.

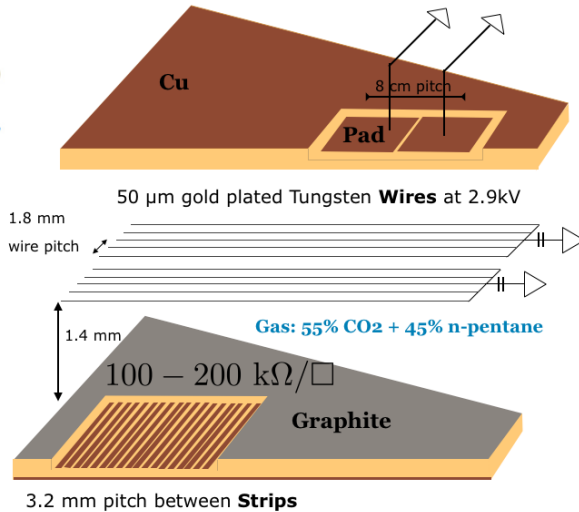


Figure 2.3: Single plane sTGC

The sTGC is made of two resistive cathodes planes, with copper readout plane with strips on one layer and the other one with pads, with $8 \times 12\text{cm}^2$ area used for fast pattern recognition of tracks to select strips for read out. This represents a big advantage compared to the TGC, which does not have this feature.

The cathodes are made of FR4 with 1.4mm of thickness, where $17\mu\text{m}$ of copper is etched for strips (pads), pressed with a $100\mu\text{m}$ of FR4 over it and then sprayed with graphite to provide superficial resistivity.

The anodes are golden tungsten wires of $50\mu\text{m}$ diameter, distributed at 1.8mm of distance between each other and a gas gap of 2.8mm. To work with such geometry, several tests were made to find the proper gas mixture[6]. The most suitable mixture has been found to be 55% (CO_2) and a quenching gas, a primary ingredient is 45% of n-pentane($\text{n-C}_5\text{H}_{12}$), which allows the chamber to work in a limited proportional region[7](see Section 1.2.3). The latest ingredient; n-pentane, can absorb UV photons due to its many molecular degree of freedom, hence preventing the chamber from going into a Geiger mode.

2.3.1. Electric field simulation

Motivated by gaining better understanding of the detector operational mechanisms, dedicated simulations studies using gaseous detector simulation tools have been performed. The main simulation tool used is Garfield [8, 9] software package. This set of libraries allows to calculate the electrical field with geometrical configuration as drift chambers.

The simulation uses a coordinate system where x is along the strips, y defines the chamber depth and z is along the wires.

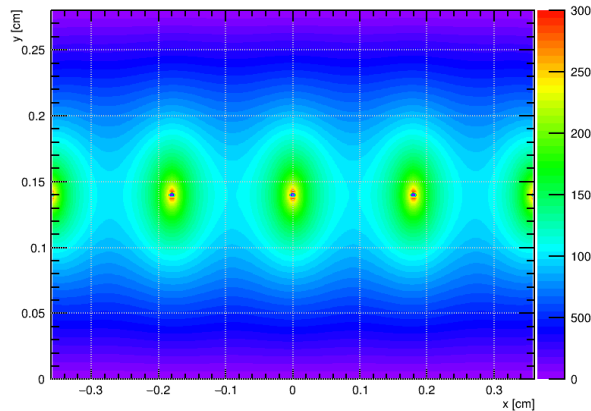


Figure 2.4: Equipontential lines, anode at 2900V

Both contour plots on figure 2.5 represent the magnitude of the electrical field with scale of $1 \times 10^3 \text{ V/cm}$ to $1 \times 10^5 \text{ V/cm}$ with 50 steps. At the working potential 2.9 kV, it is possible to observed a field strength of more than $1 \times 10^4 \text{ V/cm}$ over a 97% of the gas gap. The weakest field is only in a small region in the middle of two neighboring wires, leading to less than 5% of long drifting electrons.

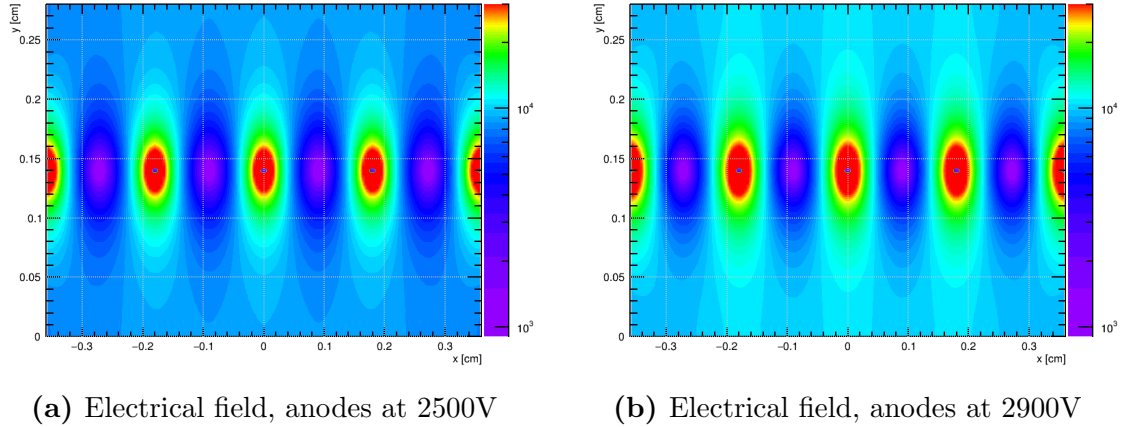


Figure 2.5: The electric field map in the x-y plane for a typical operating high voltage 2900V and 2500V.

2.4. Construction process

The main novelty on this detector is the high resolution obtained on x-axis due to the strip boards and the alignment between each chamber to get precision of about $50\mu\text{m}$ and $30\mu\text{m}$ respectively.

It is important to discuss the process which makes it possible to achieve these numbers. Everything relies on how well these chambers are built and also how the cathodes boards (strips and pads) are fabricated.

The size of each chamber varies from 0.7 m^2 to 2.5 m^2 with around 1m long, where over 300-400 strips must be etched with a precision of $50\mu\text{m}$. A standard length for printed circuit boards (PCB) is 70 cm. Extremely precautions must be taken to provide the precision and parallelism between each strips, in one of the biggest PCB board ever made.

The attempt of this section is to provide an overview of how the sTGC Quadruplets are built, mostly on the first module 0 produced by UTFSM, which is the QS1 (Quadruplet Small sector, part 1). Being the smallest detector to be produced for the NSW has some pros and cons. The main cons is related to the position of the QS1 inside the NSW; it is the closest one to the interaction point and as such, it gets the highest rate of particles. For the same reason, the position resolution is a key point and the high efficiency response under a high rate environment is a must.

Some pros are related to its size; with approximately 1.3 m long, 35 cm the small base and 75cm the large one of the trapezoidal shape, the sTGC QS1 can be handled without any problems during its construction.

Quality Control of cathode boards

The cathodes for the module 0 were made by an Italian company MDT, and since it was the first production, the review was done on-site.

The thickness of the board is measured in 19 points around the perimeter with a

micrometer. The values of these measurements must be within $1.5\text{mm} \pm 25\mu\text{m}$. Exceeding this numbers leads to the partial rejection of the cathode boards, however if there is a single point deviation of less than $35\mu\text{m}$ from the average, it could be used in combination with another cathode board that does not have the same local deviation.

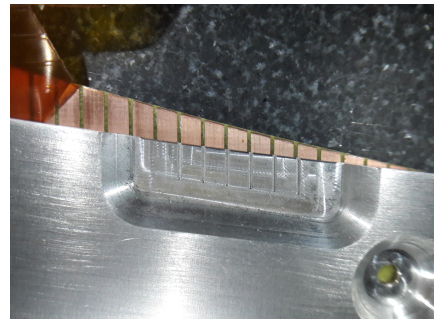
An electrical test is done with a multimeter, to check if there is any short circuit between strips or pads depending on the cathode board.

The last step and the most important is the dimensional control; it is performed on a granite table, with 2 pins that match the brass inserts on the cathode and a special caliper.

An aluminum-ruler (Al-ruler) machined (see Figure 2.6a) with a precision of $30\mu\text{m}$ at 20 Celsius degrees is used as caliper. Above the cathode board the misalignment is measured. It has the same strip pitch for the first and the last five strips as well as two intermediate regions, and to avoid any parallax, the thickness of the edge for these strips is 1mm. Looking with a magnifying glass around 4 regions allows to detect some misalignment between these strips (caliper and cathode board). A photography is taken and analyzed to calculate this misalignment. For such distance (about 1 m long) some precautions must be taken, considering the expansion coefficient for both material.



(a) Al-ruler used to check shift over the last strips.



(b) Zoom-in Comparing strip position

Figure 2.6: Strip control with Al ruler

Cathode preparation

Once the cathodes pass all the dimensional control, they have to be cleaned with Acetone and Isopropyl alcohol and placed on a granite table (with a flatness better than $30\mu\text{m}$) with a vacuum system underneath. They have to be fixed on the edges with metal jigs which have marks for the internal wire support or chamber division.

The places which are not sprayed with graphite, like the wire support and the edges, are covered with a 3.5mm black tape on the designated wire support locations across the board. To prevent spraying graphite on the places where there will be glue, a blue tape must be placed on the edges.

Graphite spraying

A key point for this process is to prepare the “painting”, a mixture of Graphite-33 with Plastik-70 bonding agent.

The graphite must be agitated for at least 2 hours before mixing with Plastik-70. A proper ratio of 1500g Graphite and 540g Plastik is mixed during 2 hours before spraying.

A spraying machine is in charge of this process, and meanwhile temperature and humidity must be controlled. After the cathode is painted, the superficial resistivity is measured on the edges. Values must exceed $100\text{k}\Omega/\square$ otherwise the cathode needs to be sprayed again.

Polishing

In order to ensure an homogeneous resistivity across the chamber, the cathode is visually divided in to 5x6 sections. Inside each section, the resistivity is measured on 5 to 7 points with a probe. Simultaneously the cathode is brushed in the same orientation as the wires. The brush must be done carefully, without over-polishing areas, because once the resistance drops down, nothing will bring it back up.

Gluing internal parts

After removing all the blue and black tapes, all the internal parts (buttons, wire support, etc.) are glued to provide mechanical support to the anode wires.

The wire support and the buttons help the chamber not to bend due to gravity and not to create a catenary effect. The external frames provide the 1.4mm height for the gas gap. All these part are cleaned with isopropyl alcohol, While the glue, a type of epoxy (2011-Araldite) is prepared, all these parts are cleaned with isopropyl alcohol. This glue will not only fix the parts, it will also fill the surfaces where these parts are less thick than requested.

Winding wires

A flat table which can spin around one axis is used to wind the cathodes board. On each side of the table, one cathode with all the internal parts is tight with metal clamps on the edges. At the same time, vacuum is applied underneath to ensure the flatness of the cathode. A winding machine places each wire at 1.8mm distance from each other with $50\mu\text{m}$ precision.

After the process is completed, all the wires are soldered in batches of 10 over the wire-rulers. The remaining wire can be cut and the HV resistors ($10\text{M}\Omega$) soldered. The metal clamps around the edges are then removed, and the relative wire tension is checked by comparing the deflection of adjacent wires.

Detector Assembly

Once the cathodes are winded and all wires are soldered, the Pad cathode board is cleaned with clean water and dried with clean air. The board is placed on the granite table

(with vacuum underneath) to be tested with high voltage. It is necessary to monitor the current from the cathode while the voltage is increased. It starts with 100V and reaches 3000V, with steps of 100V. The current should never reach a value higher than $1\mu\text{A}$. If it does, the cathode needs to be checked carefully, to remove dust or glue which create sparkles.

Reaching the nominal current, the strip cathode board is placed against the pad cathode board carefully. An aluminum frame with a silicon rubber is placed on top to isolate the chamber from the environment. Afterwards, vacuum is applied to this chamber and CO_2 is flushing inside the chamber.

The power supply is turned on and no sparkles (monitoring the current) must be found.

In order to prevent dust entering the chamber, the glue is prepared to close it immediately. Upon completion of the process, a single chamber is built.

A doublet is assembled with two single chambers glued with a honeycomb paper. Repeating the process with two doublets, the quadruplet is built.

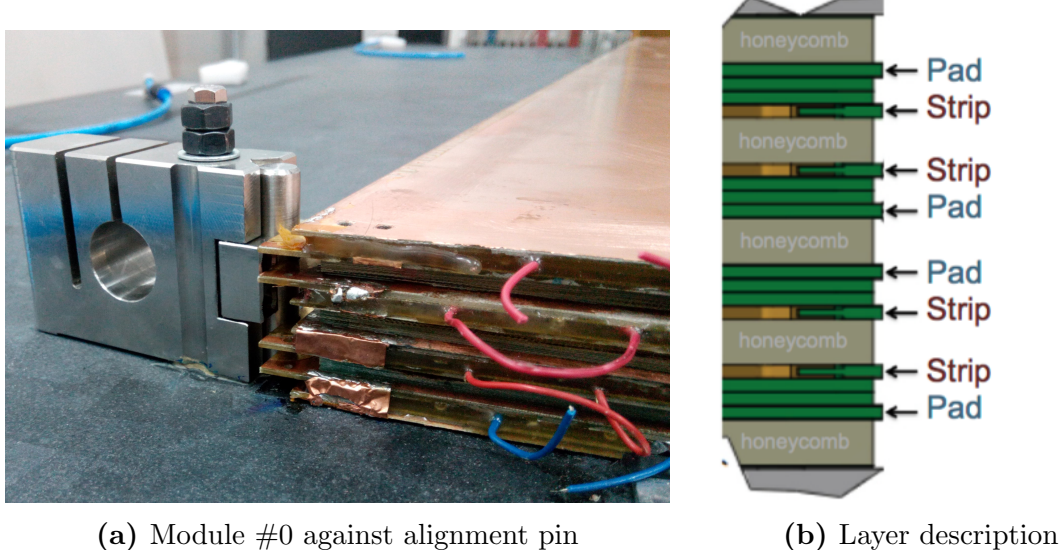
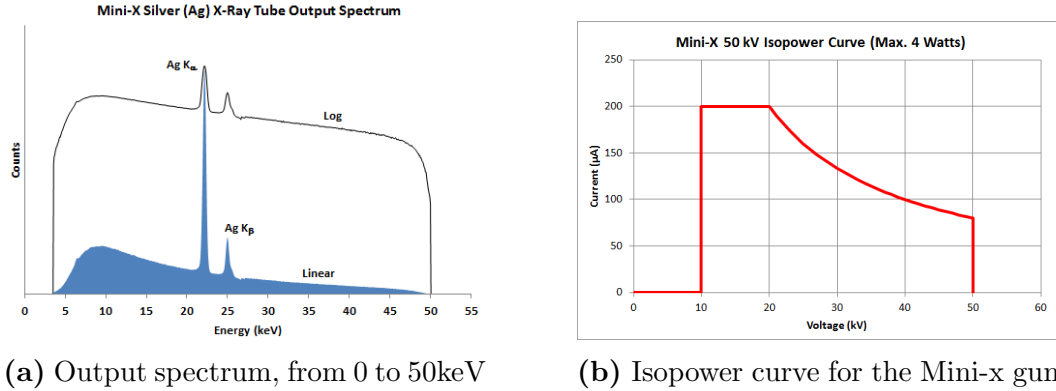


Figure 2.7

2.5. Gain uniformity measurements

After the chambers are built, it is important to look for any malfunctioning. A primitive test to check the behavior of the detector is to move a radiation source across the sensitive area, while the current draw is measured from the power supply.

In this test, it is important to understand what can produce variation on the gain. There are two main factor that can produce gain variations on wire detectors. The first one is the “nature” gain fluctuations from the charge production in proportional counters which follow Polya distribution, however it is less pronounced in limited proportional mode such as sTGC working region.



(a) Output spectrum, from 0 to 50keV

(b) Isopower curve for the Mini-x gun

Figure 2.8

The second one is related to the mechanical tolerances, this part has been very well known for 40 years as it is presented in Sauli's book [10] about drift chambers from which we can conclude the following:

- Variations on the wire diameter of about 1% (fabrication precision) results in a 3% change on the gain.
- A $100\mu\text{m}$ difference in the gas gap thickness (2.7mm) results in about 15% change on the gain.
- The effect of a wire displacement of about $100\mu\text{m}$ of a wire plane results in 1% in the charge of the two adjacent wires which with a gain of $\sim 10^6$ will give a $\sim 10\%$ change on the gain.

Taking all of this in consideration, it is expected to get a gain variation of less than 20% in agreement with the Construction manual[11].

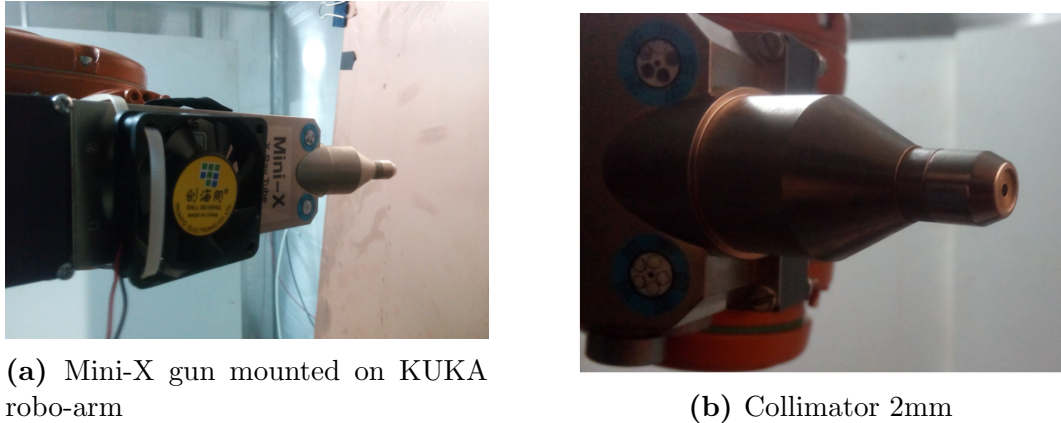
The amount of current measured from the power supply is considered as gain reference, while the detector is irradiated with x-rays. The test is performed under two different working points (bias voltage), 2500V (low gain) and 2900V, the operational voltage.

For such test the x-ray source is used due to the following advantages:

- Mostly mono-energetic photons.
- Variable photon intensity: Limiting the current from the tube from $1\mu\text{A}$ to $200\mu\text{A}$ can provide different rates.
- Variable photon energy: Varying the breaking voltage of electrons inside the x-ray gun from 10 kV to 50 kV.
- Different spot size: with a set of collimator it is possible to irradiate area of interest.

2.5.1. Setup

To perform such test, a x-ray gun called Mini-X[12] from Amptek is used, with silver (Ag) as transmission target and with a beryllium (Be) end-window.



(a) Mini-X gun mounted on KUKA robo-arm

(b) Collimator 2mm

Figure 2.9

The gun is mounted on a KUKA robo-arm (see Fig.2.9a), with a 5 degrees collimator providing a 4 mm^2 spot size at a proper distance. The robo-arm provides the x-y movement to scan the whole sensitive detector area, moving from the small base to the large base along the wires at step of 1.2 cm/s (y – axis).

The robo-arm moves along the x-axis in 5 cm/s steps. This is not the most suitable step to irradiate the whole detector, but it allows the x-ray gun to work properly at $45\text{ }\mu\text{A}$, 50 keV energy (see figure 2.8b) without overheating.

A NIM HV Power Supply Module CAEN 1470 was used to power the chambers. The power supply (PS) was controlled by USB with the CAEN HV Wrapper Library. The current registered from the PS was written in a ASCII file for further analysis. The sampling rate used from the PS was 1 per second, giving the current average during this period. The test is taken in approximately one hour, irradiating one chamber at the time.

Since the detector is already built as a quadruplet, it has to turn over to irradiate its other face. Hence, only the external layers (chambers) are irradiated directly without having an chamber to provide a screening effect.

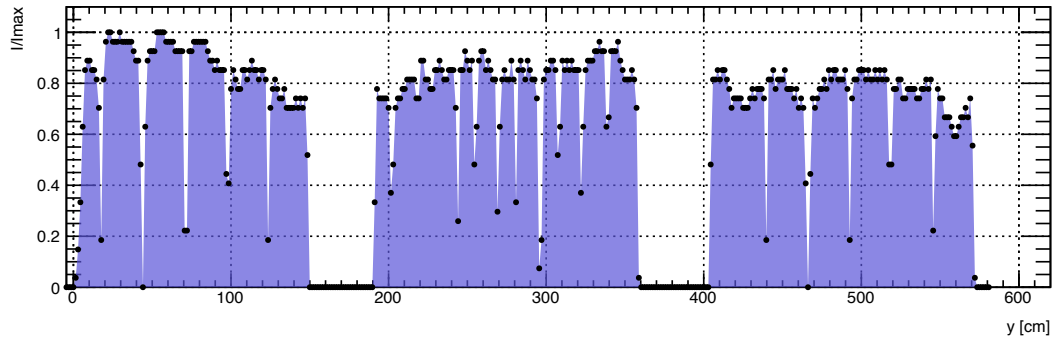
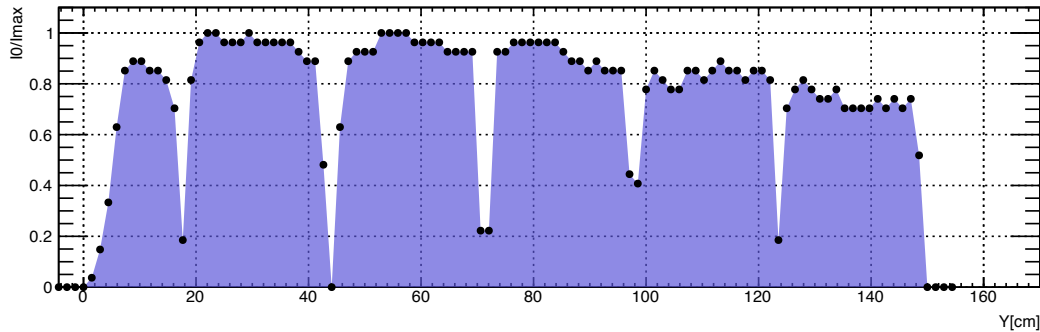


Figure 2.10: Relative current to the maximum, while the robo-arm is moved along the wires. The three set current corresponds to the whole detector irradiated in three different positions from x-axis.

	Chamber 1	Chamber 2	Chamber 3	Chamber4
$\sigma/\text{mean}\%$	15.08%	17.18%	17.25%	16.64%

Table 2.2: Uniformity gain

2.5.2. Results

**Figure 2.11:** Moving across strips, wire-supports are present with minimum gain.

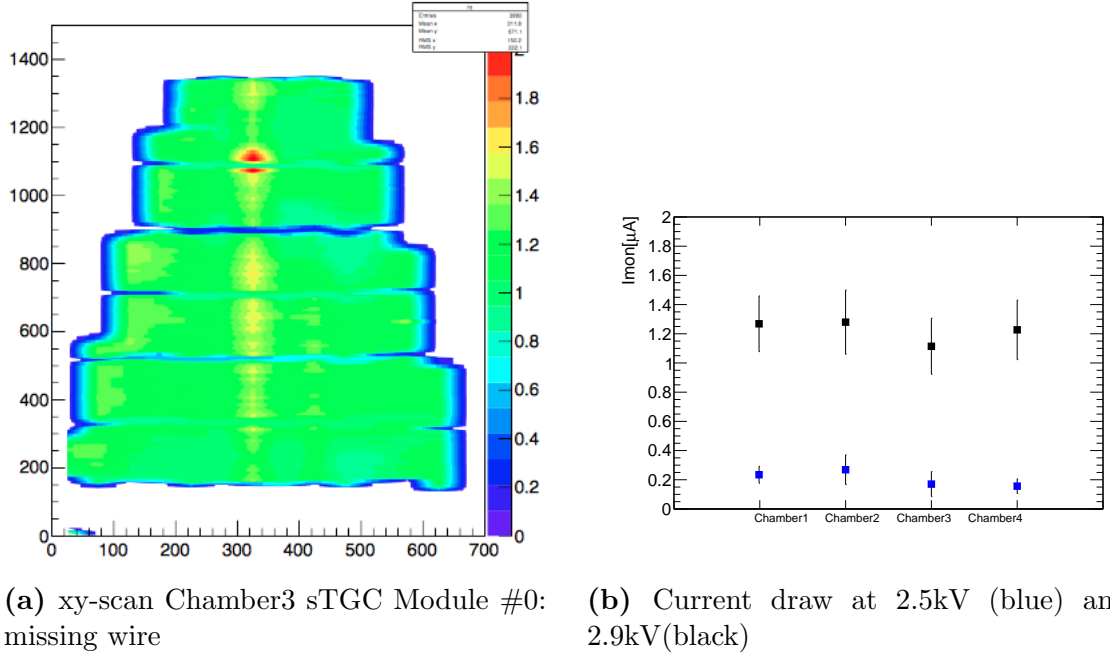
At first glance, it is possible to observed the internal structure of the chamber with this test. Looking at the Figure 2.11 the current decreases when the gun is irradiating the places where the wire-supports are found. In theses places a small gas volume is present, therefore less electrons can drift to the wires, resulting in less current draw from the power supply.

If a better meshing of the irradiation places could be performed, identification of the wire-supports and the chamber separation (small and large sector) could be obtained with good resolution. For internal parts of 20mm, a width from 17 mm to 23 mm has been obtained with this test.

Interpolating the points (x, y, I) , an overall picture can be obtained (Figure 2.12a). The figure shows a line with high current resulting from a missing wire on the Chamber3. More charge is collected by the neighbors when a wire is missing, resulting from a longer drift path.

The graph on Figure 2.12b shows the average current from each Chamber at two different working potential. The average is calculated only for the sensitive area, hence, only values where the wire-support are not present form part of the average. The average current values at 2.5kV and 2.9kV are 200 nA and 1.2 μ A respectively.

The Table 2.4 summarizes the uniformity obtained, calculated as the RMS over the mean from the current draw distribution for each chamber. The four chambers have less than 20% of gain variation, which was expected from the construction manual.



(a) xy-scan Chamber3 sTGC Module #0: (b) Current draw at 2.5kV (blue) and 2.9kV(black)

Figure 2.12

2.6. Stability under high rate

One of the key feature of this detector is that it must be able to work under high particles flow rates ($15\text{kHz}/\text{cm}^2$), and the first step is to check whether the device or its electronic components can handle this high rate.

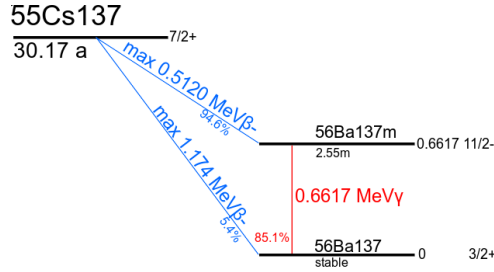


Figure 2.13: Cesium-137 Decay scheme.

For this purpose, the Module#0 was placed inside a new High Radiation Facility at CERN called GIF++[13]. The installation has a Cesium-137 (Figure 2.13) as a gamma source with an activity of approximately 14.9TBq (13.3TBq during the test, August 2016). A system of movable lead attenuators (Figure 2.14a) for large irradiation zone allows attenuation factors between 1 and 5×10^5 in several steps.

In order to get a reference of the particle rate, a direct measurement setup was implemented with a small size ($16.2\text{ cm} \times 12.4\text{ cm}$ as sensitive area) sTGC as a **Monitor**. A LVDS (Low voltage differential signaling) logical signal from wires was obtained from an Amplifier Shaper Discriminator (ASD) board[14] connected to this Monitor.

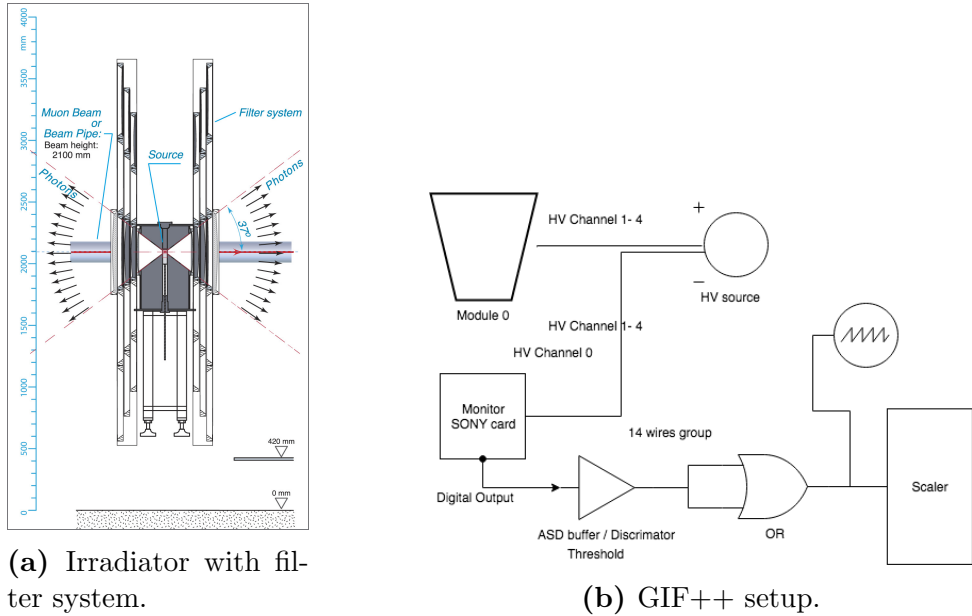


Figure 2.14: Three different rows with three lead (Pb) layers, each one with different thickness to provide multiples rates for the facility.

The ASD board provided the signal from 16 wires groups, all of them connected to a VME module (KEK ASD buffer), which controls the threshold from the discriminator on the ASD and converts the LVDS to NIM signal. The 16 LVDS signals are converted into two NIM logical signals. The two outputs from the module are connected to a Scaler NIM n145 which provides the number of positive NIM signals from the 16 channels in 10 seconds.

The Module#0 and the Monitor were placed at 1.3m distance from the radioactive source. Both were connected in series to the same gas line (55CO_2 : 45 n-pentane), and the temperature and pressure were recorded to keep track of the working voltage. Most of the time, the environmental conditions were measured at 25 Celsius degree and 971mb.

The working potential for the chamber is 2850V at 1b. Since the gain is proportional to E/P , where E is the electrical field and P the pressure inside the chamber, the voltages must be decreased by 2.9% to compensate the lower pressure, resulting in a 2765V as the new working point in this environment.

To achieve the background rate for ATLAS ($15\text{kHz}/\text{cm}^2$), the Monitor must register more than 2680 kHz if the sensitive area is considered. The sensitive area is calculated as the total area 200 cm^2 times the amount of wires group connected to the ASD.

Four different attenuation factors were registered (10, 4.5, 2.2 and 1). On Figure 2.15a it is possible to observe two sets of data with rates over than the expected one (red and blue). The other two sets of data emphasize the *plateau* reached over 2.7 kV. At the same time, the highest rate shows an inefficiency on voltages over 2.8 kV and the *plateau* is lost. Therefore, the data set with attenuation 2.2 (in red) is our reference.

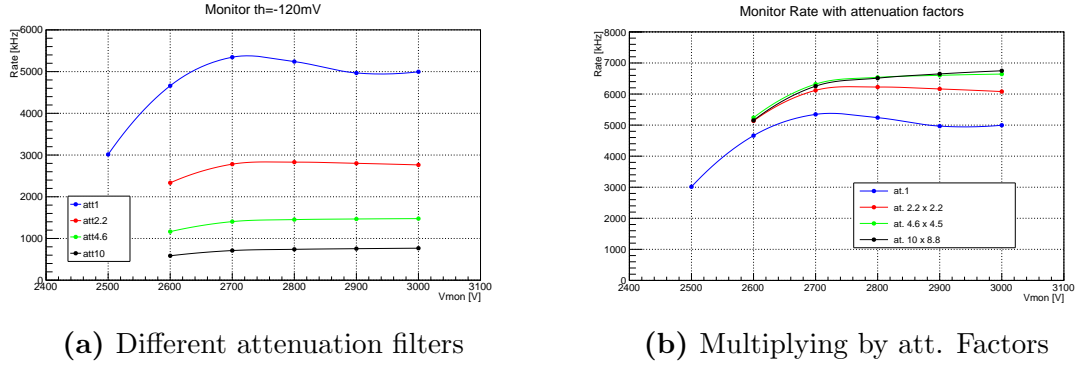


Figure 2.15: Rate on Monitor

Multiplying the attenuation factors with each data set (Figure 2.15b) should give us the expected rate with no filters. However, the data set with factor 1 has 5 MHz at working potential (2.9kV), while the expected rate from data sets attenuation 10 and attenuation 4.6 is 6.6 MHz. When comparing the rates from data set 1 with these, we observe an efficiency of about 75% of the expected rate. Then, comparing the data set 2.2 with the lowest rates results in approximately 93% of efficiency.

These findings may suggest a change in the gamma spectrum emitted after the attenuation filters. For a comprehensive analysis, a detailed study of the spectrum can be found in Chapter 3.

The flow rate recorded in data set 2.2 is 28 kHz/cm^2 , if we compensate the inefficiency the total flow rate is 30 kHz/cm^2 , which is the double than expected as a background level for ATLAS. Therefore the STGC detectors must be tested against attenuation factor lower than 4.4.

Once the Monitor is set, the quadruplet is connected to the high voltage power supply. Each layer is internally divided in two sections, a small sector (S0) and large sector (S1). Each one of these sectors is powered independently on each channel from the CAEN High Voltage power supply A1833P (4 kV/2 mA max). The current from each layer (two sectors each one) was recorded with a resolution of $0.1 \mu\text{A}$. Four different attenuation filters were applied, and the results are shown in Figure 2.16.

$$\Delta\% = \left| 1 - \frac{I_1/I_0}{A_1/A_0} \right| * 100 \quad (2.1)$$

These results shows a linear dependency of voltage, with lower resistance as the rate of particles is increased. It is also important to notice that each wire group is connected to a $10 \text{ M}\Omega$ resistor, however not all the wires have the same length (the chamber has a trapezoidal shape), resulting in a lower voltage drop from the external groups where the wires are shorter (collecting less charge).

The Table 2.3 compares the area ratio between the internal sections of each chamber with the current registered for each set of measurements. The effect of dropping voltage appears to be the explanation of the incremental disagreement of the area ratio as the rate increases.

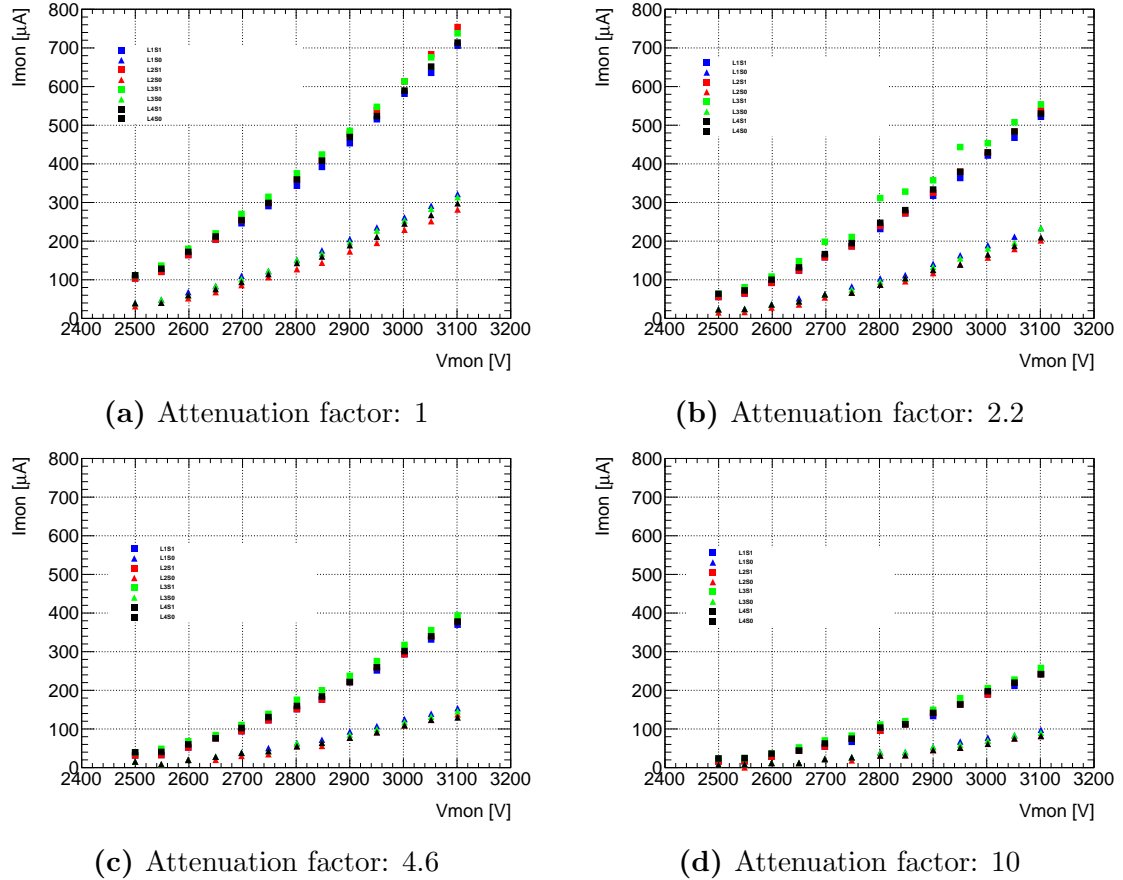


Figure 2.16: Current registered on the power supply for each chamber, large (S1) and small sector (S0) against applied voltage on anode.

The set of graphs shown in Figure 2.17 highlights the disagreement between different working voltages for two different rates.

These two sets of data are the expected rates for the large and small sector on the sTGC QS1. Hence, it is important to compare these ratios with the amount of current registered by both sectors. As the area ratio increases, the current ratio decreases, which suggests the use of different HV resistors for the external wires groups to produce an homogeneous voltage drop.

A_1/A_0	Layer 1		Layer 2		Layer 3		Layer 4		
	Filter	I_1/I_0	$\Delta\%$	Filter	I_1/I_0	$\Delta\%$	Filter	I_1/I_0	$\Delta\%$
10		2.49	1.58		3.02	8.63		3.01	1.95
4.6		2.34	7.51		2.87	3.24		2.73	11.07
2.2		2.29	9.49		2.79	0.35		2.68	12.70
1		2.22	12.25		3.02	8.63		2.45	20.19

Table 2.3: Comparison between sensitive area ratio (A_1/A_0) from large and small sectors with the ratio of current (I_1/I_0) at 2.9kV. A percentage difference column ($\Delta\%$ defined in equation 2.1) is calculated to highlight the incremental disagreement as the gamma rate and the area ratio increases.

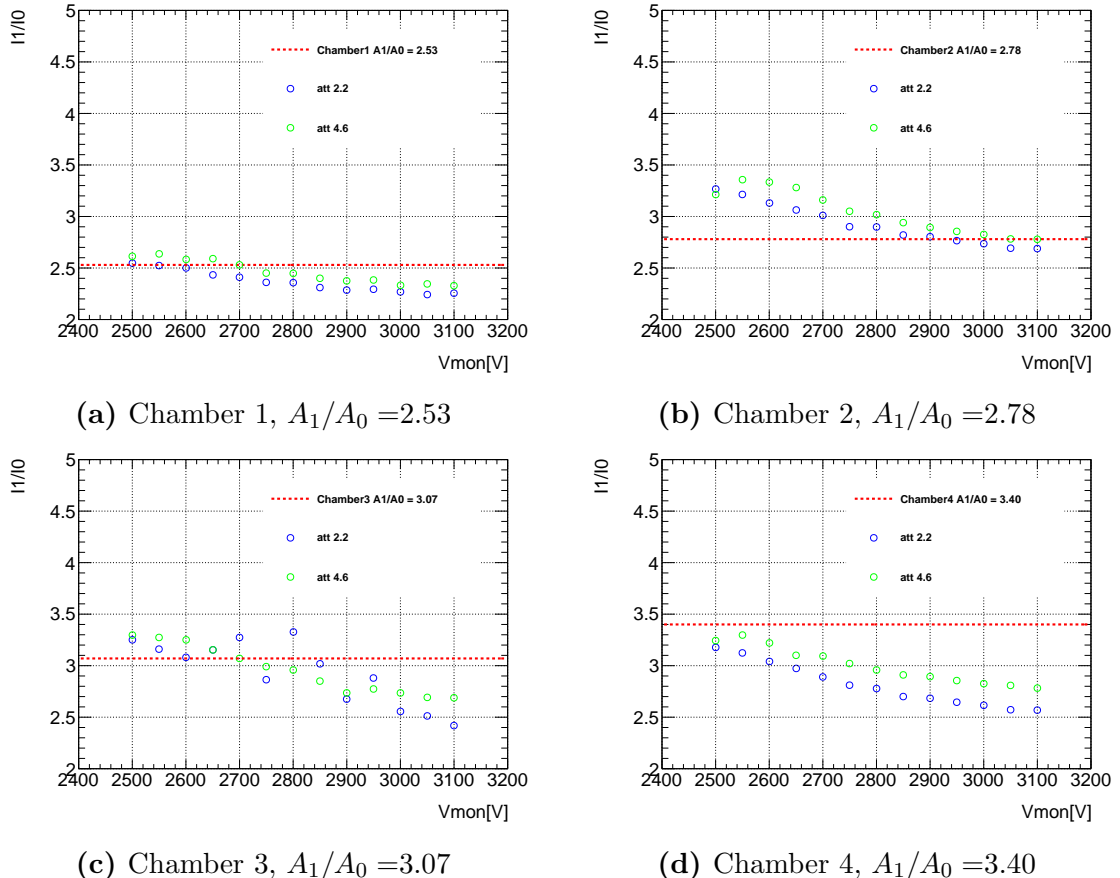


Figure 2.17: Current ratio I_1/I_0 for two different rates compared with the area ratio A_1/A_0 at different anode voltage. The Chamber 3 in (c) has a missing wire in the large section (A_1), therefore the area ratio must be slightly lower and an increase of the current can be expected for the same reason.

2.7. Spatial Resolution

In order to achieve the precision reconstruction of tracks (offline) with a spatial resolution of about $100\mu\text{m}$ per sTGC layer, and fast trigger on the region of interest (ROI) with Pads, two test beams were done.

In the spring of 2014, the Weizmann Institute of Science in Israel built the first full-size sTGC quadruplet detector of dimensions $1.2 \times 1.0\text{m}^2$. This prototype consists of four sTGC strips and pad layers and is constructed using the full specification of one of the quadruplets to be used in the NSW upgrade (the middle quadruplet of the small sector). The first test beam experiment took place at Fermilab with one goal in mind, to determine the position resolution of a full-size sTGC.

EUDET pixel telescope was used as a reference to measure the beam position, using the technology of 6 Minimum Ionizing MOS Active Pixel Sensor (Mimosa26) detectors with $\approx 5\mu\text{m}$ position resolution. Three telescopes are placed in front of the beam, and three after the sTGC as is shown in Figure 2.18 with 15cm between them and 64cm between each arm. Each Mimosa26 detector has an active area of 2.24cm^2 made of CMOS pixel matrix of 576 rows and 1152 columns with $18.4\mu\text{m}$ pitch.

A 32GeV pion beam was used at the rate of 1kHz over a spot of 1cm^2 giving to the sTGC a very precise pion trajectory thanks to the EUDET telescope. Event triggering was controlled by a custom Trigger Logic Unit (TLU). The TLU received signals from two $1 \times 2\text{cm}^2$ scintillators placed in front and behind the telescope. The TLU generated the trigger signal that was distributed to the telescope and the sTGC readout electronics, which consists of a first application-specific integrated circuit (ASIC) called VMM1 which has the ability to read out both positive (strips, pads) and negative (wires) polarity signals, on 64 individual readout channels.

The VMM1 analog circuit features a charge amplifier stage followed by a shaper circuit and outputs the analog peak value (P) of the signal.

The readout of the ASIC is zero suppressed and thus only peak values of channels with signals above a predefined threshold are read. At the same time, the VMM1 may be programmed to provide the input signal amplitude of channels adjacent to a channel above threshold (neighbor-enable logic).

The precise position of a charged particle traversing an sTGC gas volume can be estimated from a Gaussian fit to the measured charge on adjacent readout strips (referred to as strip-clusters from here on). Given the strip pitch of 3.2mm and sTGC geometry, charges are typically induced on up to five adjacent strips.

The spatial sampling of the total ionization signal over a small number of readout channels means that a precise knowledge of each individual readout channel baseline is necessary in order to achieve the best possible measured spatial resolution.

The baseline of each individual readout channel was measured by making use of the neighbor-enabled logic of the VMM1 and its internal calibration system.

Test pulses were sent on one readout channel with the neighbor-enabled logic on, and baseline values were obtained by reading out the analog peak values of the two channels adjacent to the one receiving a test pulse.

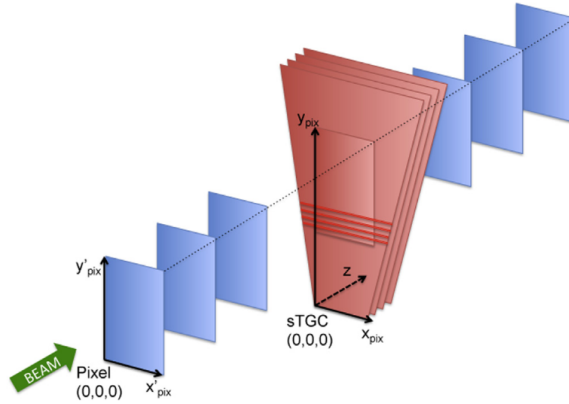


Figure 2.18: Schematic diagram of the experimental setup at Fermilab and coordinate systems used. Three layers of silicon pixel sensors are positioned before and after the sTGC detector. The dimensions are not to scale.

The silicon pixel hit positions were then used for reconstructing straight three dimensional charged-particle tracks. A track quality parameter was obtained for each fitted pion track based on the χ^2 of the track-fit. A small value of the track quality parameter corresponds to a straight track and a cut on this parameter can therefore be used to mitigate multiple scattering which are not considered in this analysis.

2.7.1. Analysis Model

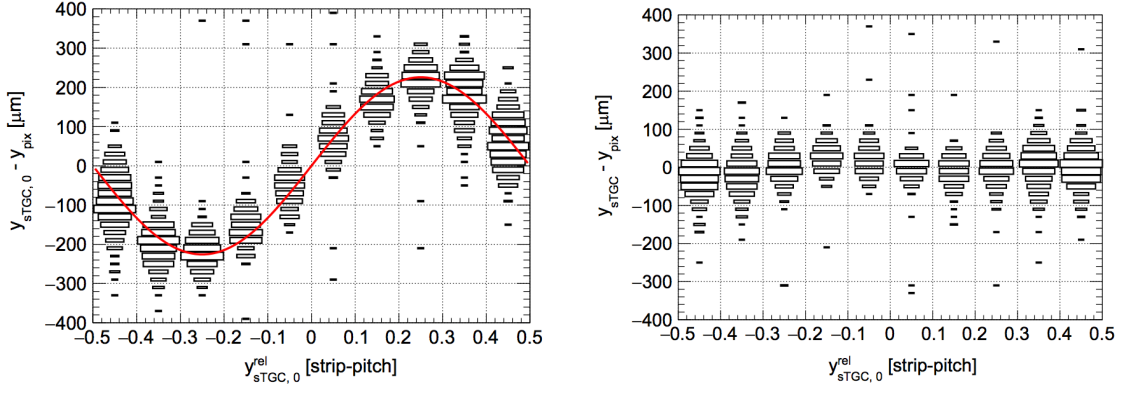
Pixel telescope analysis

In this model the intrinsic position resolution is obtained comparing the extrapolated beam trajectory from the pixel detectors with the measurements in each of the sTGC quad planes. Each layer is analyzed separately to reduce the effect of the multiple scattering and only tracks with $\chi^2 < 10$ are considered for the same reason. From Figure 2.18 one can see that the y -axis is defined perpendicular to the strips, therefore sTGC strip-clusters provide measurements of the particle position in the y -direction (y_{sTGC}).

The position resolution is directly related to the profile of induced charge on the strips. The particle position is estimated from a Gaussian fit to the induced charge distribution on the strips. The neighbor-enabled logic of the VMM1 was used. Strip-clusters with induced charge in either 3, 4 or 5 adjacent strips are selected.

The pixel telescope tracks provide both coordinates, x_{pix} and y_{pix} at the position of the sTGC layer studied. The spatial resolution measurement is obtained by fitting the residual distribution y_{sTGC} and y_{pix} with a Gaussian model.

The charge measured on the strips of the sTGC detector results from a spatial sampling and discretization of the induced charge. The process of reconstructing the sTGC strip-cluster position from this sampling introduces a differential non-linearity effect on the reconstructed strip-cluster position.



(a) The differential non-linearity for sTGC strip-clusters
 (b) The differential after sinusoidal correction is applied

Figure 2.19: Charge distribution over strip-pitch

Table 2.4: Fit parameters per cluster size

Strip-cluster multiplicity i	Amplitude parameter a_i
3	205 ± 9
4	206 ± 4
5	211 ± 5

The deviation of the measured strip-cluster position from the expected position (estimated by the pixel telescope track) depends on the strip-cluster position relative to the strips. This dependence is clearly seen in the two dimensional distributions in Figure 2.19a. It shows the y-residual versus strip-cluster position relative to the closest inter-strip gap center $y_{\text{sTGC},0}^{\text{rel}}$. This effect is corrected using a sinusoidal function:

$$y_{\text{sTGC}} = y_{\text{sTGC},0} - a_i \sin(2\pi y_{\text{sTGC},0}^{\text{rel}}) \quad (2.2)$$

where $y_{\text{sTGC},0}$ is the strip-cluster mean resulting from the Gaussian fit and y_{sTGC} is the corrected particle position estimator. The amplitude parameters are denoted a_i for the 3,4 and 5 strip-multiplicity (cluster size). These amplitude parameters are free parameters in the fit. The values of the amplitude parameters obtained from the fit to data are compatible with being equal for the three strip-cluster multiplicity as shown in Table 2.4.

The correction function is therefore universal and is shown in Figure 2.19a. The two dimensional distribution after the correction is applied was found to be reasonably flat as shown in Figure 2.19b.

The alignment of the coordinate system of the pixel telescope with respect to the above-defined coordinate system of the sTGC layer also affects the measured residual distribution. A simple two-parameter model is used to account for translations and rotations of the two coordinate systems with respect to each other. Both the alignment correction and the differential non-linearity correction are included *in situ* in the analysis.

The alignment correction is introduced in the model by expressing the pixel track position in the sTGC-layer coordinate system y_{pix} , as a function of the track position in

the pixel telescope coordinate system x'_{pix} and y'_{pix} , and two misalignment parameters δy and ϕ_{xy} , as follows:

$$y_{\text{pix}} = -x'_{\text{pix}} \sin \phi_{xy} + y'_{\text{pix}} \cos \phi_{xy} + \delta y \quad (2.3)$$

The variable δy corresponds to a misalignment along the y-axis of the sTGC coordinate system, and ϕ_{xy} corresponds to a rotation of the telescope coordinate system in the x-y plane around the z-axis of the sTGC coordinate system. Translation and rotation misalignment along and around the other axis are not taken into account in this model, since they are expected to have a small impact on the determination of the intrinsic position resolution.

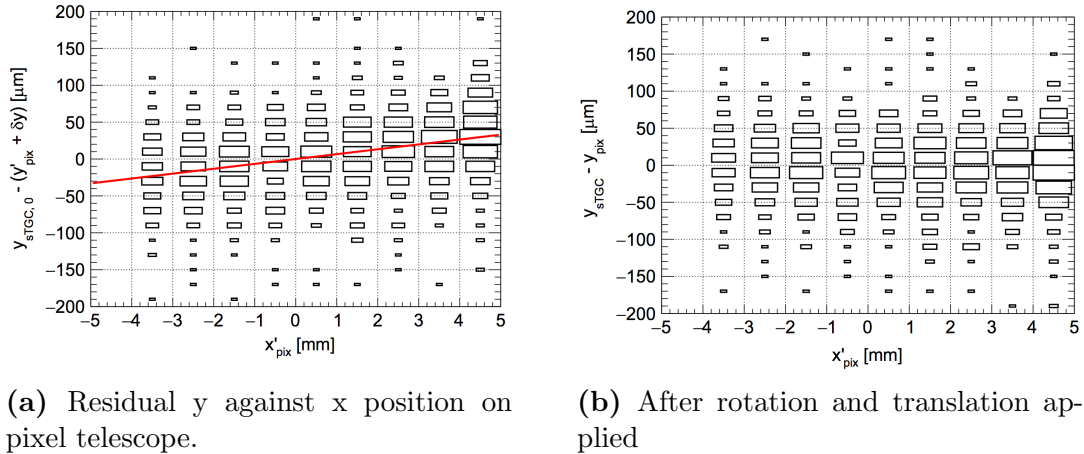


Figure 2.20: Coordinate system correction

On the Figure 2.20a it is possible to observe the y-residual mean increase linearly as a function of the x position on the telescope called x'_{pix} , which is evidence for a small rotation between the two coordinate systems. The red line represents the correction applied to this dataset. Accounting for this correction results in a distribution that is independent of x'_{pix} on Figure 2.20b.

After all the corrections are applied, the calculations for the intrinsic resolutions are taken for each layer and compared with the residual distribution. A double Gaussian function (equation 2.5) is fitted, where the first Gaussian represents the core of the residual distribution and the second one is a wider Gaussian which represents some reconstructed strip-cluster from background sources.

$$F_i = F_i(y_{\text{STGC,0}}, y_{\text{STGC,0}}^{\text{rel}}, x'_{\text{pix}}, y'_{\text{pix}}; \delta y, \phi_{xy}, a_i, \sigma, f, \sigma_w) \quad (2.4)$$

$$= fG(y_{\text{STGC}} - y_{\text{pix}}; 0, \sigma) + (1 - f)G(y_{\text{STGC}} - y_{\text{pix}}; 0, \sigma_w) \quad (2.5)$$

On Figure 2.21 a set of events shows the distribution presented before with an intrinsic resolution parameter σ of about $44\mu\text{m}$ for a representative data taking run and sTGC strip-layer, where the red line is the narrow Gaussian fit and the dashed line is the wider Gaussian fit.

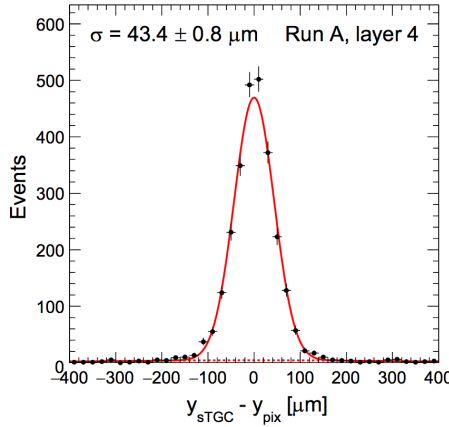
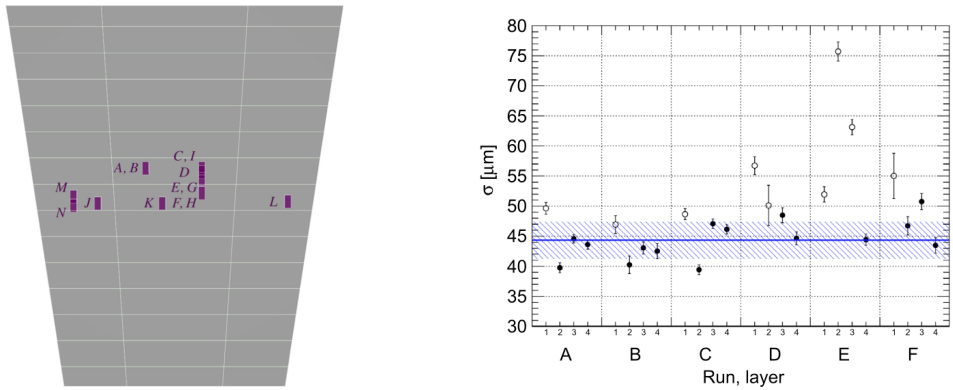


Figure 2.21: Intrinsic resolution of layer 4, respect to pixel telescope.



(a) Beam position for different data sets on sTGC

(b) Summary of intrinsic resolution for each data set and layer of sTGC

Figure 2.22: Summary of pixel telescope analysis

The fraction of the data parameterized by the narrow Gaussian is around 95% with a RMS of about 2%. The rest of data taking runs and its beam position can be observed on Figure 2.22b, where the black circles represent the valid data and the open circles the runs with expected degradation due to detector structure supports or individual channel pedestal.

sTGC standalone analysis

In this analysis the correction for the differential non-linearity in respect to strip-pitch obtained before is kept, however the residual distribution of the y-position is calculated from two pairwise layer of the sTGC. Therefore half of the variance of this distribution corresponds to our parameter to estimate the intrinsic resolution for one layer, hence $\sigma = \sigma_{\text{residual}}/\sqrt{2}$.

A strip-layer position residual distribution for a representative sTGC standalone data taking run is shown in Figure 2.23a.

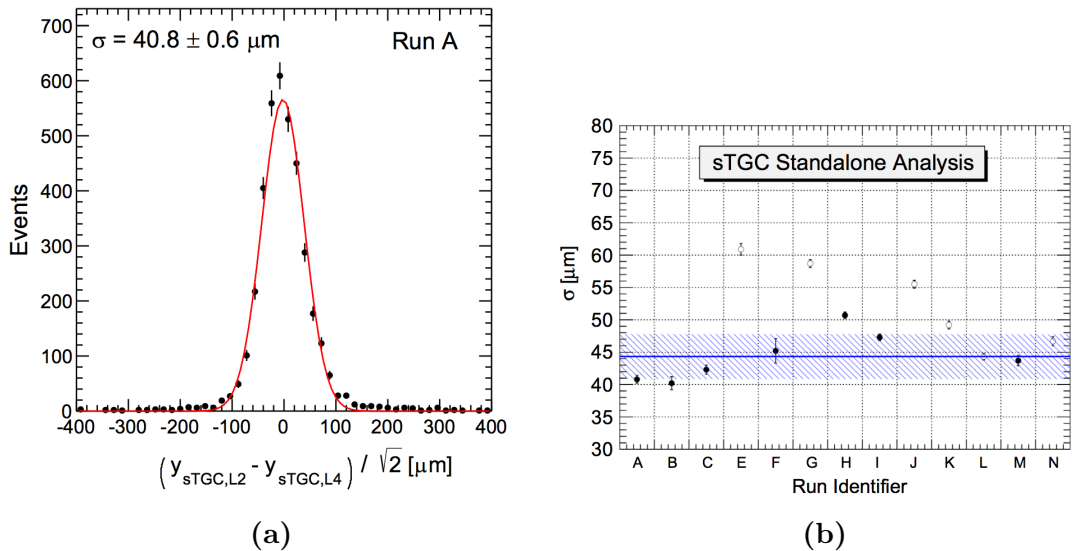


Figure 2.23: (a) Resolution estimate based on adjacent sTGC strip-layer position residual distributions for a representative sTGC standalone data taking run.

(b) Summary of the measured intrinsic sTGC resolution using the pixel telescope analysis for different data taking runs. The beam position on the sTGC detector for each run is shown in 2.22a. Results for runs with no expected degradation due to sTGC detector support structure or calibration are shown as black filled circles. The horizontal line represents the average resolution for these runs whereas the hashed band represents the RMS spread. Results for the remaining runs are shown as open circles.

In this graph, a intrinsic resolution of $\sigma = 40.8 \pm 0.8 \mu\text{m}$ is obtained.

In summary of fourteen data sets, the intrinsic resolution with this analysis is about $45 \mu\text{m}$. The white open circles on the graph 2.23b correspond to non-validate data due to wire-support position or mis-calibrations. The hash band represents the RMS spread and the blue line is the average.

2.8. Pad efficiency

One of the new features of the small-strip Thin Gap Chamber compare to its previous version is the possibility to provide a fast trigger for the Region of Interest from the $8 \times 50 \text{ cm}^2$ pad area, where 3 out of 4 pads from a sTGC quadruplet can confirm a particle candidate, therefore a track position can be obtained from the strips within this area.

A test beam experiment was conducted at the CERN H6 beam line, using a 130 GeV muon beam of about 4 cm radius, a wider beam spot to test the characteristics of the pads. The setup is shown in Figure 2.24 where the system was triggered by a set of scintillators (in blue) with a $12 \times 12 \text{ cm}^2$ coincidence area.

As explained before, for the beam tests a preliminary front-end electronics based on

the VMM1 was used. This ASIC provides a Time-over-Threshold (ToT) signal as digital output, however is also possible to get analog pulses. During the test beam, using the present configuration, an inefficiency was observed related to small late charges from the sTGC detector which may be not well adapted to the VMM1. An efficiency of 80-90% was observed running at 100 kHz/cm².

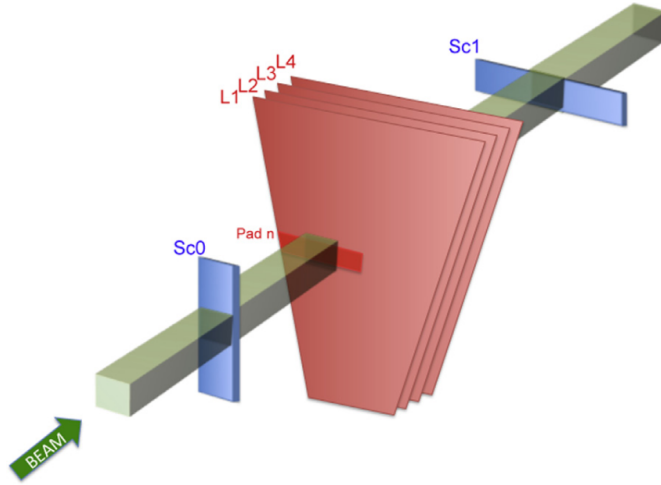


Figure 2.24: Setup for pad measurements. Coincidence block in light green. Pad n in red. Scintillators in blue.

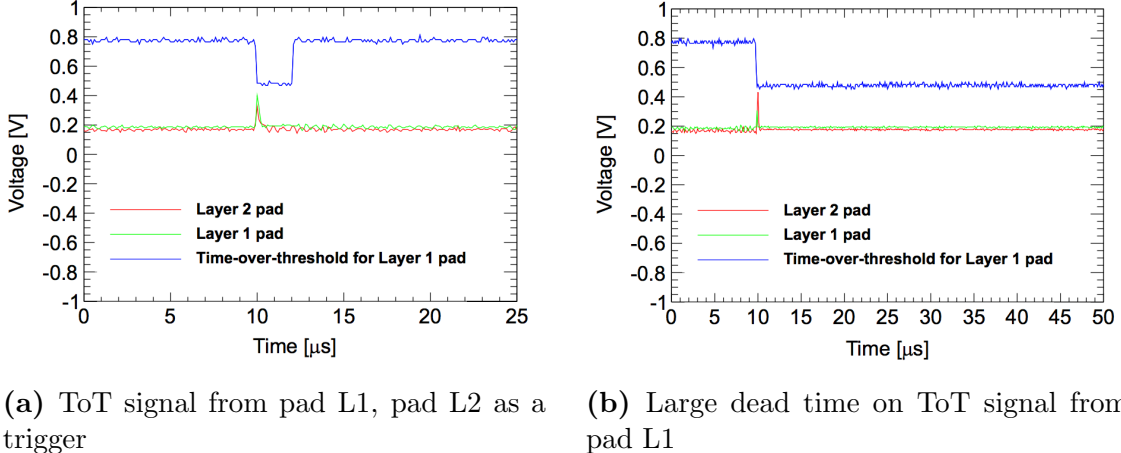
To ensure that no inefficiency was due to the detector itself, the large cathode pads were used to estimate the detector efficiency, which was measured by looking at the analog output of the front-end amplifier. The efficiency of the pad n in the first layer was defined with respect to the coincidence of the trigger with a signal in the fully overlapping pad of the second layer.

Two examples from this configuration are shown on Figure 2.25; on the left a two analog signals from pads are present with a ToT signal from layer 1 with about 2 μ s length, meanwhile on the right picture a long ToT pulse with more than 40 μ s length when the two analog signal are present. By recording hundreds of triggered events using an oscilloscope, the presence of a detector signal within the live-part of the front-end electronics (independent of the signal threshold) was checked. This test confirmed that the detector was 100% efficient.

Charge sharing between pads

To study the transition region between pads, the scintillator coincidence triggering area and the particle beam were centered between pad n and pad $n + 1$ of the first layer, as illustrated in Figure 2.26a.

After applying timing quality requirements on the strip and pad hits, the channel baseline values are subtracted from the analog peak values. Strip-clusters with induced charge in either 3,4 or 5 adjacent strips are selected and calibrated in the same way as for the Fermilab beam test.



(a) ToT signal from pad L1, pad L2 as a trigger
 (b) Large dead time on ToT signal from pad L1

Figure 2.25: Digital and analog signal from VMM1

Events with a single strip-cluster in the first layer and the second layer are selected. The strip-cluster position (mean of the fitted Gaussian) in the first layer is used to define the position of the particle going through the detector. The events are further required to contain a hit above threshold on either pad n or pad $n + 1$. The charge fraction (F) is defined using the analog peak values (P) of the two adjacent pads:

$$F = \frac{P_n - P_{n+1}}{P_n + P_{n+1}} \quad (2.6)$$

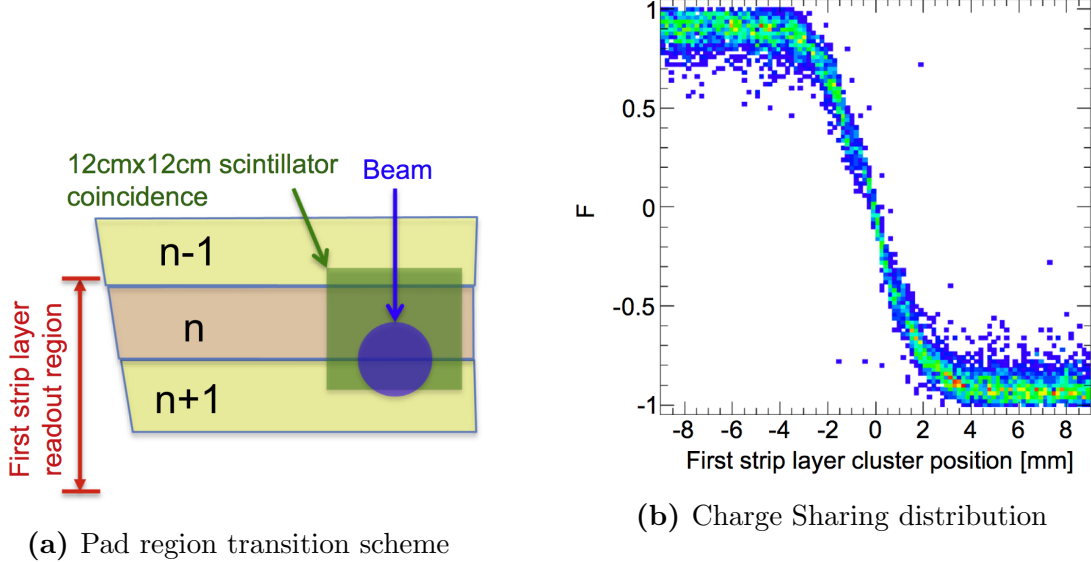


Figure 2.26

Figure 2.26b shows the charge fraction as a function of the position with respect to the center of the transition region, where the two pads share more than 70% of the induced charge, spans about 4mm.

2.9. Summary

In the chapter we introduce the construction process and discuss the phenomenology of the sTGC. The main features of this Thin Gap Chamber are presented. The smaller strips of 3.2mm pitch give the spatial resolution needed for the improvement of the New Small Wheel of ATLAS. The main problem to achieve this precise $3.2\text{mm} \pm 50\mu\text{m}$ pitch in long boards (1m to 2m long) is discussed.

To improve the time response the resistivity of the graphite layer is decreased and the distance between the readout and graphite layer is reduced to a $100\mu\text{m}$.

The sTGC detector is tested with four different objectives. The first test under x-rays occurs right after the Quadruplet is constructed. The use of this source helps to understand the construction issues as well as qualifying process, where the uniformity of the gain is measured.

Certainly, multiple factors can be improved in this test, such as increasing the vertical and horizontal steps to benefit from the 2mm spot size of the x-ray gun. Although the entire process for this test can be improved, the Module#0 shows an overall 17% uniformity for the four chambers.

In the Section 2.6 a direct measurement of the rate in a high irradiation environment is provided by a small size sTGC. The references values obtained help to set a working point to test the new Quadruplets against high flow rate. The non-linear change in the resistivity of the chamber for different particles rates suggests a better election for the resistor component connected to the anode wires. All the group wires are connected in series to a $10\text{ M}\Omega$, however, not all the groups receive the same amount of charge in an homogeneous particle rate because of the different lengths in the trapezoidal shape of the sTGC.

The last two sections summarize the two test beams for the first sTGC prototype, where crucial results are obtained for the electronics in charge of the readout. The test beam in CERN helps to understand the inefficiency of the Pads. The electronics designed for this detector (VMM1) has some issues which provides a 80-90% efficiency running at 100 kHz/cm^2 . The detector is discarded, therefore, the VMM1 needs to be improved.

On the sTGC technology, all the efforts go to the improvement of the position resolution and the Section 2.7 shows a intrinsic resolution of about $40\mu\text{m}$ for the standalone analysis.

The spatial resolutions and pad efficiency results have been published in “Performance of a full-size small-strip thin gap chamber prototype for the ATLAS new small wheel muon upgrade” [15].

The estimation of the position and efficiency resolution as a function of background rates inside the high rate environmental with a muon beam is remaining and it will be done after a new version of the VMM1 electronics is produced.

3. High count rate γ -ray spectroscopy in GIF++

3.1. Introduction

- Problem faced in chapter 2, with high radiation facility.
- Explain the attempt to get reference about this issue
- Device to be used BriLLance 380
- characterization

3.2. Counter Limit

Limit of pulse recognition, refer paper high rate...

3.3. High Radiation Source

Description of Cesium source, flow estimation for GIF++,

3.4. Data Analisys

3.4.1. Multiple hits

how to handle it?

3.4.2. Wavelets

Introuction to Wavelets
Discrete Wavelet Transform

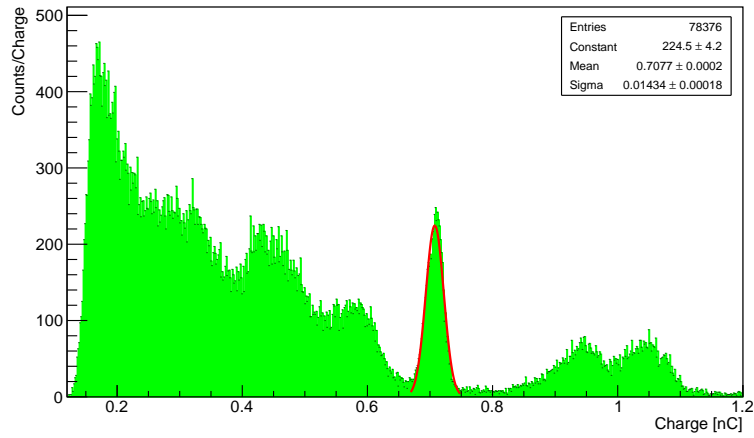


Figure 3.1: Selfcount spectrum

3.4.3. Peak identification

Chosing Wavelet function for peak identification
Heavy ion paper, peak identification

3.5. Results

Show multiple pulse in window, and peak identification, cases...

3.5.1. Spectrum

Spectrum for different rates (attenuation filters)
Spectrum with multiple pulse, using peak identification and pattern recognition.

3.5.2. Gamma Flux Rates

Rate estimation, compare with gain and rate measured with Scaler.

4. Synchrotron radiation detector for e^- tagging

Many high energy experiments require pure electron beams. Despite the steady improvement of the beam lines, contamination below a level of few % is very difficult to achieve. An example is the NA64 experiment[16] at CERN in which it is mandatory to suppress hadron and muon contamination in the electron beam since such particles can generate irreducible background processes mimicking the experimental signature of a dark photon [17, 18]. NA64 uses 100 GeV electrons from beam lines provided by the Super Proton Synchrotron (SPS) at CERN which is one of the best existing beam lines at this energy in terms of beam purity[19].

Since the electrons are secondary particles from the proton beam at the SPS, the experiment uses magnets to remove the remaining hadrons (pions and kaons) and some low-energy electrons from the interaction with passive material along the beam line. For this reason, the experiment use the synchrotron radiation to tag the incoming electrons and reject the other events.

In this chapter we start by briefly describing the NA64 experiment goals and the advantage of it. The experiment has two different configuration for two possible dark photon decays, *visible* and *invisible*. These two configurations are discussed, however, the focus goes on the *invisible decays*, where results are shown.

To detect a dark photon signal, the level of hadron contamination must be reduced to the level of 10^{-5} without compromising the electron efficiency below 95%. For this purpose, the experiment posesse three different options of synchrotron radiation detectors (SRD).

A brief discussion of why is not possible to use the Cherenkov radiation as particle identification process is presented. While the synchrotron radiation is the key for this range of energy.

Results from BGO crystal detector are compared with a more complex device. This modern device take the advantages of a new type of scintillator assambled in an array of 625 crystals. Thanks to the short decay time from this material can help to work under the highest electron beam intensity from the SPS beam line.

Finally the results from dark missing energy events of dark photons in the invisible mode configuration are presented.

4.1. NA64 experiment

The NA64 experiment is a fixed-target experiment at the CERN SPS combining the active beam dump and missing energy techniques to search for rare events.

A fully hermetic detector placed on the H4 beam line has been built with the primary goal to search for light dark bosons (Z') from dark sector that are coupled to photons, e.g. dark photons (A'), or sub-GeV Z' coupled only to quarks. In some cases the Z' is coupled only to μ or τ , so we call the Z' the dark leptonic gauge boson. The experiment is also capable to search for $K_L \rightarrow \text{invisible}$ decay, which is complementary to $K^+ \rightarrow \pi^+ + \nu\nu$, and invisible decays of π_0 , η , η' , K_S mesons.

The advantage of this approach is that the sensitivity (or number of signal events) of the experiment is roughly proportional to the Z' coupling squared ε^2 , associated with the Z' production in the primary interaction in the target, while in a classical beam dump experiment, it is proportional to ε^4 , one ε^2 came from the Z' production, and another ε^2 is either from the probability of Z' decays or their interactions in a detector located at a large distance from the beam dump.

The sensitivities of these two methods depend on the region under study in the $(\varepsilon^2, m_{Z'})$ parameter space, background level for a particular process, available beam intensity (Figure 4.1), etc.

In some cases, much less running time and primary beam intensity are required to observe a signal event with our approach.

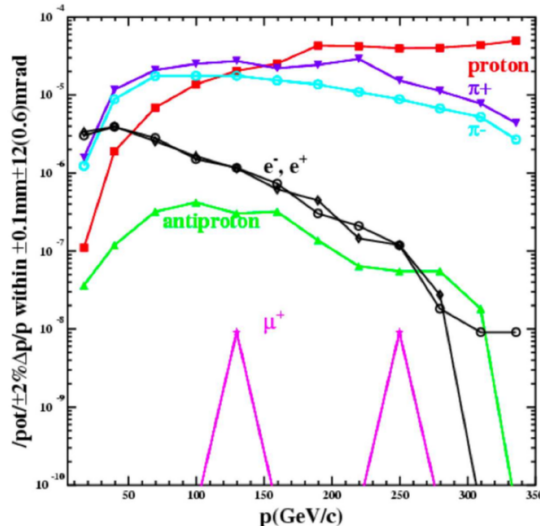


Figure 4.1: Beam intensity of H4 beam line from target T2 at SPS, CERN.

One of the main background sources in the experiment is related to the possible presence of the low-energy tail in the energy distribution of beam electrons. This tail was observed during irradiation of the setup by the 100 GeV electron beam without switching on the deflecting magnet. This tail is caused by the electron interactions with a passive material, e.g. as entrance windows of the beam lines, residual gas, etc... Another source of low energy electrons is due to the pion or muon decays in flight in the beam line.

The uncertainties arising from the lack of knowledge of the dead material composition in the beam line are potentially the largest source of systematic uncertainty in accurate calculations of the fraction and energy distribution of these events. Hence, the sensitivity of the experiment could be determined by the presence of such electrons in the beam, unless one takes special measures to suppress this background. To reject these background sources at high energies by using standard techniques, e.g. threshold Cerenkov counters, is practically impossible, see Section 4.2.1.

To improve the high energy electrons selections and suppress background from the possible admixture of low energy electrons, we use a tagging system utilizing the synchrotron radiation (SR) from high energy electrons in a dipole magnet, installed upstream of the detector.

4.1.1. Physics Motivation

$$\mathcal{L} = \mathcal{L}_{SM} - \frac{1}{4} F'_{\mu\nu} F'^{\mu\nu} + \frac{\epsilon}{2} F'_{\mu\nu} F^{\mu\nu} + \frac{m_{A'}^2}{2} A'_\mu A'^\mu + i\bar{\chi}\gamma^\mu \partial_\mu \chi - m_\chi \bar{\chi}\chi - e_D \bar{\chi}\gamma^\mu A'_\mu \chi \quad (4.1)$$

Standard Model.

$g_\mu - 2$ muon anomaly

4.1.2. Dark Photon signal

U(1) broken symmetry \rightarrow massive dark photon
type of mixing coupling constant and sub-GeV mass connect with $g2$ muon anomaly. How to detect him?

Visible decay

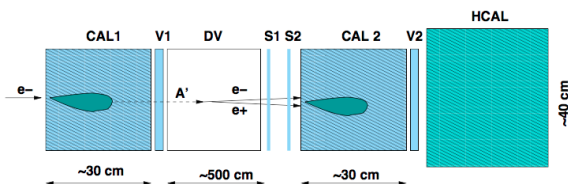


Figure 4.2

$$S_{A'} = \text{CAL1} \cdot \bar{V1} \cdot S1 \cdot S2 \cdot \text{CAL2} \cdot \bar{V2} \cdot \text{HCAL} \quad (4.2)$$

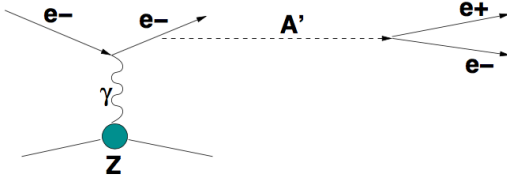


Figure 4.3: Diagram illustrating the massive A' production in the reaction $e^-Z \rightarrow e^-ZA'$ of electrons scattering off a nuclei (A, Z) with the subsequent A' into an e^+e^- pair.

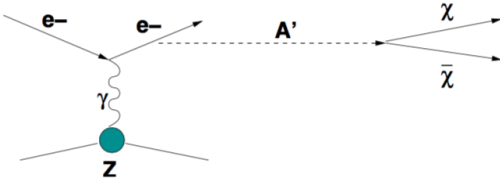


Figure 4.4: Production rate at H4 beam line

Invisible decay

The method of the search is the following. The incident electron energy absorption in the ECAL is accompanied by the emission of bremsstrahlung A' 's in the reaction $eZ \rightarrow eZA'$ of electrons scattering on nuclei, due to the $\gamma - A'$ mixing. The diagram for the A' production in the reaction is shown in Figure 4.4.

The reaction typically occurs in the first few radiation length (X_0) of the calorimeter (ECAL0). The part of the primary beam energy is deposited in the ECAL, while the remaining fraction of the total energy is transmitted by light dark matter decay particles χ through the rest of the detector. The χ penetrates the ECAL, veto V and the HCAL without interactions resulting in the missing-energy signature in the detector.

The occurrence of $A' \rightarrow \text{invisible}$ decays produced in e^-Z interactions would appear as an excess of events with a single electromagnetic shower in the ECAL1, Fig. 4.5, and zero energy deposition in the rest of the detector (V and HCAL), above those expected from the background sources. The signal candidate events have the signature:

$$S_{A'} = H1 \cdot H2 \cdot \text{ECAL}(E_{\text{ECAL}} < E_0) \cdot \bar{V} \cdot \text{HCAL} \quad (4.3)$$

and should satisfy the following selection criteria:

- The momentum of the incoming particle track should correspond to the beam momentum.
- The starting point of (e-m) showers in the ECAL should be localized within a few first X_0 's.
- The lateral and longitudinal shapes of the shower in the ECAL are consistent with an electromagnetic one. The fraction of the total energy deposition in the ECAL is

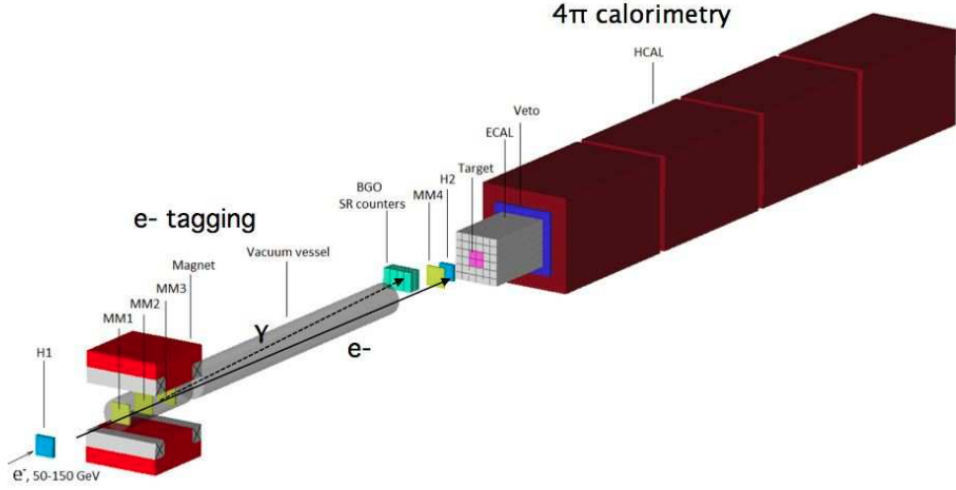


Figure 4.5: Illustration of detector configuration for Invisible decays of Dark photon.

$$f < 0.5.$$

- No energy deposition in the V and HCAL.

To improve the primary high energy electrons selection and additionally suppress background from the possible presence of low energy electrons in the beam typically with energy $E_e < 0.5E_0$ (see below), one use a high energy e^- tagging system utilizing the synchrotron radiation (SR) from high energy electrons in a dipole magnet, as schematically shown in Fig. 4.5.

4.1.3. Detector

The A' production is a rare event. For the interesting parameter range it is expected to occur with a rate 10^{-9} with respect to the ordinary photon production rate. Hence, its observation represents a challenge for the detector design and performance.

The experimental setup specifically designed to search for the A' production in the reaction (4) of high-energy electron scattering off nuclei in a high density target T is schematically shown in Fig. 3. The experiment employs the upgraded H4 electron beam line at the CERN SPS described in details in Ref.[19]. The beam is designed to transport the electrons with the maximal intensity $\simeq (3 - 4) \cdot 10^6$ per SPS spill in the momentum range between 50 GeV/c to 150 GeV/c that could be produced by the primary proton beam of 450 GeV/c with the intensity up to a few 10^{12} protons on target. The electrons are produced by protons impinging on a primary beryllium target and transported to the detector inside the evacuated beam-line tuned to an adjustable beam momentum.

The hadron contamination in the electron beam is $\pi/e < 10^{-1} - 10^{-2}$ and the size of the beam at the detector position is of the order of a few cm^2 .

The detector shown in Figure 4.6 utilizes upstream magnetic spectrometers (MS) consisting of dipole magnets and a low-material-budget tracker, which is a set of Micromegas

chambers , MM1-MM4 (T1-T4 in the figure), allowing the reconstruction and momentum resolution at 100 GeV $\Delta P/P \sim 2\%$ for incident electrons [20]. It also uses the scintillating counters S0, S1 and hodoscopes H1 and H2 to define the primary beam, and the active target T, which is the central part of the high-efficiency hodoscopic electromagnetic calorimeter (ECAL) used for the accurate measurement of the recoil electron energy from the reaction (4). Downstream the target the detector is equipped with high-efficiency forward veto counter V, and a massive, completely hermetic hadronic calorimeter (HCAL). Three straw-tubes chambers, MUON1-MUON3, located between the HCAL modules are used for the final-state muon(s) identification. The modules serve as a dump to completely absorb and detect the energy of hadronic secondaries produced in the electron interactions $e^- A \rightarrow \text{anything}$ in the target. In order to suppress backgrounds caused by the detection inefficiency the HCAL must be longitudinally completely hermetic [18, 19]. To enhance its hermeticity, the HCAL thickness is chosen to be $\simeq 30\lambda_{\text{int}}$ (nuclear interaction lengths). The 15 m long vacuum vessel between the magnet and the ECAL is installed to avoid absorption of the synchrotron radiation photons detected at the downstream end of the vessel by the array of BGO crystals for the effective tagging of the incoming beam electron.

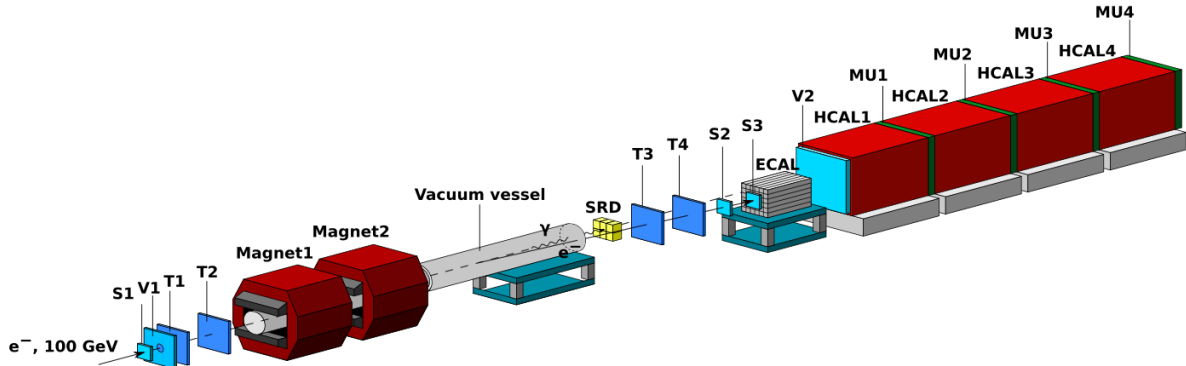


Figure 4.6: Schematic illustration of the setup to search for $A' \rightarrow \text{invisible}$ decays with 100GeV e^- at H4 beam line. the incident electron energy absorption in the ECAL is accompanied by the emission of *bremsstrahlung* A 's in the reaction $eZ \rightarrow eZA'$ of electron scattering on nuclei, see Diagram interaction. The part of the primary beam energy is deposited in the ECAL, while the remaining fraction of the total energy is transmitted by the decay dark matter particles through the rest of the detector resulting in the missing energy signature in the detector.

4.2. The synchrotron radiation tagging system

The basic idea is that, since the critical SR photon energy is $(\hbar\omega)_{\gamma}^c \propto E_0^3$, the low energy electrons in the beam could be rejected by using the cut, e.g. $E_{\gamma} > 0.3(\hbar\omega)_{\gamma}^c$, on the energy deposited in the SR detector.

One of the main background sources in the experiment is related to the possible presence of the low-energy tail in the energy distribution of beam electrons. Indeed, this tail was immediately observed during irradiation of the setup by the 100GeV electron beam without switching on the deflecting magnet (see Figure 4.7). This tail is caused by the electron interactions with a passive material, such e.g. as entrance windows of the beam lines, residual gas, etc... Another source of low energy electrons is due to the pion or muon decays in flight in the beam line.

The uncertainties arising from the lack of knowledge of the dead material composition in the beam line are potentially the largest source of systematic uncertainty in accurate calculations of the fraction and energy distribution of these events.

An estimation shows that the fraction of events with energy below $\lesssim 10\text{GeV}$ in the electron beam tuned to 100GeV could be as large as 10^{-8} . Hence, the sensitivity of the experiment could be determined by the presence of such electrons in the beam, unless one takes special measures to suppress this background.

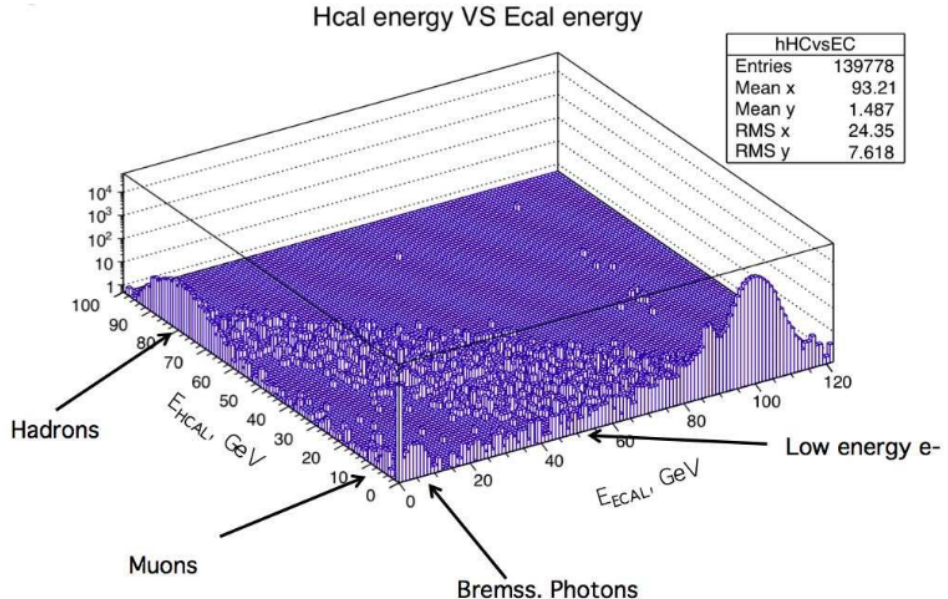


Figure 4.7: Distribution of 100GeV e^- events in the $(E_{\text{HCAL}}; E_{\text{ECAL}})$ plane.

4.2.1. Cherenkov Radiation

To reject these background sources at high energies by using standard techniques, such as threshold Cherenkov counters, is practically impossible. The use of Cherenkov radiation allows to identify the particles by their mass. This type of electromagnetic radiation is emitted when a charged particle passes through a dielectric medium at speed v greater than the phase velocity of light c/n , where n is the refraction index of the medium. Hence, the condition to emit Cherenkov radiation is when:

$$\frac{v}{c} = \beta > \frac{1}{n} \quad (4.4)$$

In a beam line, the particles are selected by their momentum P , therefore particles with different mass would have the same momentum. For a relativistic particle the velocity β can be written in terms of its momentum and total energy E :

$$\beta = 1/\sqrt{1 + (m/P)^2} \quad (4.5)$$

where m is the mass of the particle. Therefore, the selection of the particles (with different mass) can be done changing the threshold of Cherenkov radiation using a proper medium with a refraction index n which allows the selection from β_1 and β_2 . The medium selected must have a refraction index n such as $\beta_1(m_1) > 1/n$ and $\beta_2(m_2) < 1/n$, where $m_1 > m_2$. But for a 100GeV momentum $\beta_\pi \simeq \beta_e$ and an index refraction which satisfy the condition $\beta_1 > 1/n_{max}$ where $n_{max} \simeq 1.0000000979$ and should be higher than $n_{min} \simeq 1.0000000001$ thus the method is inefficient for this range of energy.

4.2.2. Synchrotron Radiation

Another technique to reject heavy charged particles is the use of synchrotron radiation which exploit the high suppression of the radiated power emitted by particles heavier than electrons passing through a magnetic field in order to discriminate them. The use of this technique is not new and detection of electrons or positrons in electrons beams with momenta ranging from 30 to 50 GeV was reported earlier by [21, 22, 23].

For synchrotron radiation we understood when a charged particle in a magnetic field moves in a circular motion emitting photons along its trajectory due to the basic principles of electrodynamics. Both quantum and classical theory of synchrotron radiation (SR) are well understood [24]. In the range of interest for our experiment both treatments are equivalent and we can therefore use the classical approximation for our calculations. The total power P emitted per unit length by a relativistic charged particle of energy E with mass m and with bending radius R in a magnetic field B perpendicular to its velocity is given by:

$$P = \frac{q^2 c}{6\pi} \frac{1}{(mc^2)^4} \frac{E^4}{R^2} \quad (4.6)$$

where q is the charge of the particle and c the speed of light. Since the emission angle of the synchrotron is proportional to the inverse of the Lorentz factor γ , the photons are emitted tangentially to the particle trajectory.

Hence under a circular acceleration, an charged particle, e.g. an electron, emits synchrotron radiation and the energy radiated per particle per turn being

$$\Delta E = \frac{e^2 \beta^3}{3\epsilon_0 R} \left(\frac{E}{mc^2} \right)^4 \quad (4.7)$$

Putting the numerical values for ϵ_0 and e , and setting $\beta = 1$

$$\Delta E = 0.08856 \frac{E^4}{R} \quad (4.8)$$

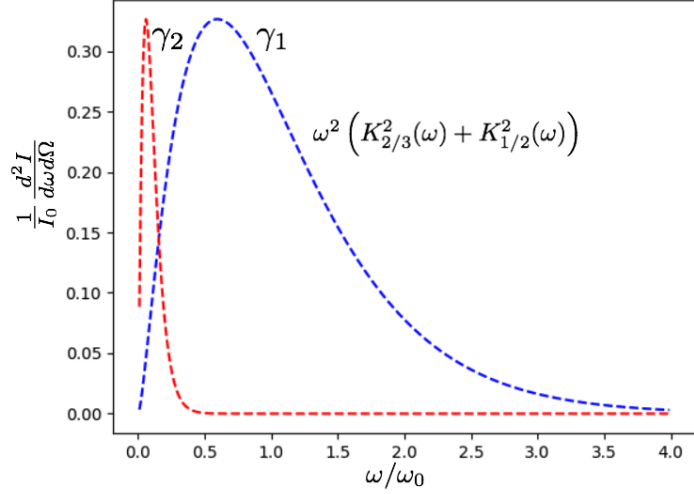


Figure 4.8: Spectrum synchrotron radiation from two different particles, where $\gamma_1 = 10\gamma_2$

where ΔE is in MeV, E is in GeV and R is in meters. Thus for relativistic π^- 's and e^- 's of the same energy, the energy loss is $(m_e/m_{\pi^\pm})^4 \sim 10^{-10}$ times less for a π^\pm . This would be the case if the particles propagate in an ideal vacuum. However, in a real experimental setup, vacuum windows, residual gas, beam counters such as scintillators and trackers result in interactions of the incoming particles with material. Therefore, the suppression factor when crossing materials is limited by the emission of secondary electrons with enough kinetic energy (several MeV) to leave a synchrotron-like signal in the detector. Although most of the energy transfer due to ionization for heavy charged particles is only a few keV, rare high energy transfer is possible. The distribution of such secondary electrons with kinetic energy $T \gg I$, where I is the mean excitation energy of the atom/molecule, for a particle with velocity β and charge z passing through a material with atomic number Z , mass number A and thickness dx is described by PDG.

$$\frac{d^2N}{dTdx} = \frac{1}{2} K z^2 \frac{Z}{A} \frac{1}{\beta^2} \frac{F(T)}{T^2} \quad (4.9)$$

The constant K is defined as $K = 4\pi N_A r_e^2 m_e c^2$ where N_A is the Avogadro's number, r_e is the classical electron radius and m_e the electron mass. $F(T)$ is a spin-dependent factor, which in our case for $T \ll W_{max}$ is very close to unity. W_{max} is the maximal energy transfer in a single collision to the electron:

For a π^- at GeV, W_{max} is roughly 1GeV which covers completely the energy range where synchrotron radiation is emitted.

For 100GeV electrons in the $B = 1.7\text{T}$ bending field this corresponds to $E_c \sim 11.35\text{MeV}$. The expected mean energy of a synchrotron photon $E_m = E_c/\pi \simeq 3.6\text{MeV}$ is in very good agreement with simulation. The number of photons emitted per revolution in this energy range in the field of $7\text{T}\cdot\text{m}$ is defined as:



Figure 4.9: The scheme of the additional tagging of high energy electrons in the beam by using the electron synchrotron radiation in the bending magnetic dipole. The synchrotron radiation photons are detected by a γ -detector by using scintillator as BGO crystals, LYSO crystals or a different configuration with Pb+Sc. All these options are viewed by a high quantum efficiency PMT or SiPM. The beam defining counters are also shown.

$$N_{\gamma's} = \frac{5\pi\alpha}{\sqrt{3}}\gamma \quad (4.10)$$

where α is the fine structure. By scaling this equation for the fraction of the circle where the particles are inside the magnetic field, one obtains a mean number of emitted photon of about 24. Afterwards we should consider the geometrical acceptance of the SRD to estimate the total energy deposited in the detector.

To detect this SR, the experiment has been working to find the best suitable detector. For this task three options has been tested, three type of scintillator material; BGO, LYSO and Pb+Sc. Each of one with different geometry and crystal's configuration. On this thesis we focus only on two out of the three options, BGO and LYSO due to its similarities and good perfomance. A description of these detector can be found on the next sections and a comparison of how can be used to suppress the hadron contamination on the beam line.

4.2.3. BGO

The NA64 experiment, use as a first option of SRD an array of $\text{Bi}_4\text{Ge}_3\text{O}_{12}$ (BGO) crystals because of its high photoelectric gamma rays absorption and a configuration that can the detect the incoming SR and reject the back scattering event coming from the ECAL.

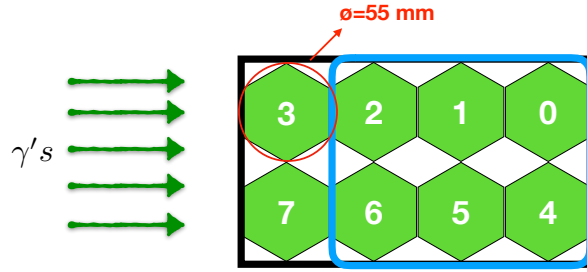


Figure 4.10: Detector BGO, array of 8 hexagonal crystals with 55mm external diameter and 200mm length. .

The detector consists of 8 hexagonal crystals with an external diameter of 55 mm and a length of 200 mm (see Figure 4.10). The first two crystals collect most of the synchrotron radiation spectrum. The last two crystals are affected only in case of a high energy event and rare thus uses as a veto. The remaining crystals (square light blue) serve as a shield for the SRD from backscattering particles coming from the ECAL. The crystals are grouped into two modules. Each crystal is wrapped in Teflon tape for efficient light collection and it is glued to an ETL 9954 photomultiplier(PMT).

The BGO crystal has a density of 7.13 g/cm^3 and because of the high atomic number of the bismuth component ($Z = 83$) it has one of the largest probability per unit volume for photoelectric absorption of gamma rays. [25]. The light yield of about 8500 γs/MeV coupled to the transportation losses and quantum efficiency of the PMT gives an energy resolution of about 17% (FWHM) at 1.27 MeV (measured with a ^{22}Na radioactive source).

4.2.4. LYSO

The setup for invisible decays has different scintillating material to detect synchrotron radiation. An array of LYSO[26] crystals. This array consists of 25×25 crystals of $4 \times 4 \times 45 \text{ mm}^3$ each crystal is a Cerium doped lutetium ($\text{Lu}_{1.8}\text{Y}_{0.2}\text{SiO}_5 : \text{Ce}$), with a light output of 35.000 [photons/MeV]. This type of crystals has a short time decay (see Table 4.1) compared to BGO crystals. Therefore, it is a more suitable candidate for a SR detection at high rates. With a decay time of $\tau = 40\text{ns}$, allows to a maximal electron counting rate of $\lesssim 1/\tau \sim 10^7 e^-/s$.

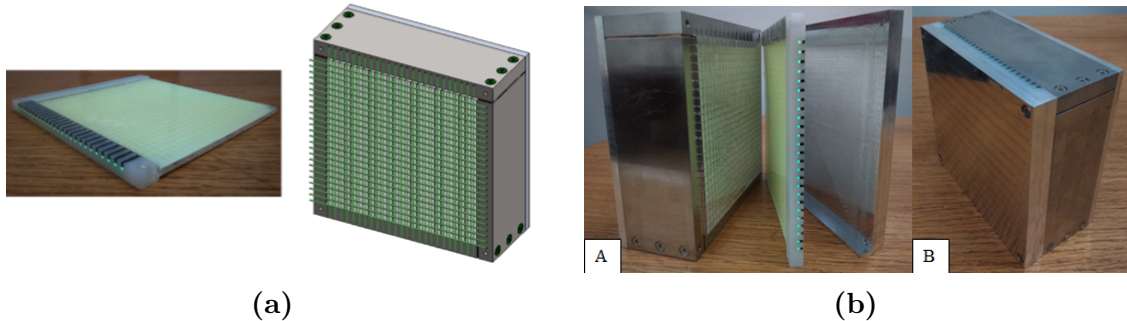
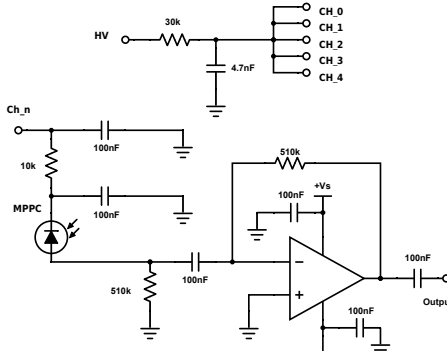
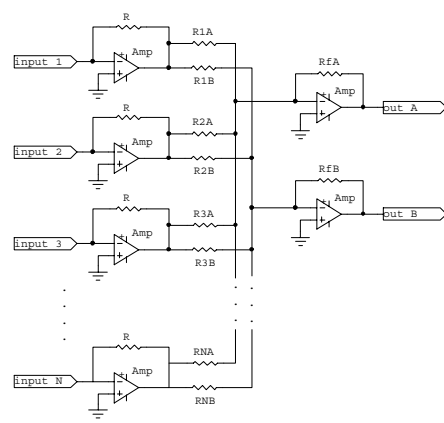


Figure 4.11: LYSO detector

Property	LYSO	BGO
Density [g/m ³]	7.1	7.1
Attenuation length for 511 keV [cm]	1.2	1.0
Decay time [ns]	41	300
Energy Resolution %	8.0	12.0
Light output, photons per keV	32	9
Radiation Length	1.16	0.96

Table 4.1: Property comparison LYSO and BGO crystals

(a) Amplifier and bias voltage circuit for MPPC



(b) Weighted signal circuit

Figure 4.12: The figure (a) shows two circuits, one the amplifier circuit (bottom) for each Multi-Pixel Photon Counter. On top is the common bias voltage for 5 channels. The circuit on (b) provides the two weighted signal from N channels which is implemented on one side of this detector to reduce the amount of channels.

The light spectrum emission from LYSO crystals has its peak at 420 nm, this light is collected from a net of KURARAY Y-7 wave length shifter (WLS) fibers. This WLS has its maximum of light absorption at 439nm and 490nm of its peak emission. The net of fibers are mounted in a UVT acrylic (see Figure 4.11a) and at the end of each WLS there is a small light guide connected to a Multi-pixel photon counter (Hamamatsu S10931-025P) to measure the photons collected. This type of Avalanche photo diode is perfect for the emission of the WLS due to its photon detection efficiency (PDE) maximum (50%) is close to 490nm.

Each crystal is wrapped in a ultra high reflective film Vikuiti and assembled in an aluminum housing as shown the Figure 4.11b. The light collection is taking only from one side from this array. On Figure 4.11b is possible to observe the end of each 25 fibers from one side. Once the housing is closed the electron readout are mounted on top and on one side of this box shape. This design of about $4X_0$ can be used as a preshower detector with a compact volume and high dense transversal segmentation.

Readout

The readout consists of 50 Multi-pixel Photon Counter (MPPC) [27], distributed into 25 per axis (X and Y). The 25 MPPC from each axis were selected to share the same bias voltages in group of 5 with similar gain. However the signal output comes from the 25 photon counters. The Figure 4.12a shows the amplification circuit for each MPPC and the circuit which connect the 5 neighbor MPPC to the same bias voltage.

The high transversal segmentation (4mmx4mm) from this device can help to identify the particle position and its energy very accurate. However, its disadvantage is the amount of channels need it for this purpose.

The lack of free ADC channels in the NA64's DAQ system lead us to reduce the channel numbers. Since the electron beam will be deviated only horizontally, the SR accros should be homogenously distributed across the x-axis. Therefore, to identify other events, with low SR emission like pions or delta electrons it is much better to keep the advantage of the 25 channels. On the other hand, the use of a charge division readout system on the y-side can help to reduce from 25 to two analog output signals.

This readout system operates as a multi-channel analog signal converter which converts signals from multi-channel output position sensitive devices to two per coordinate analog outputs with same amplitude correlation as common charge division position readout.

For the experiment NA64, the readout was downgrade from 50 to 27 channels. 25 from the X axis were kept and 2 weighted signals are obtained from 25 channels from Y axis. Two main reasons lead us to the this downgrade, the first one is due to the limited number of channels of the DAQ system, and the second one is there is no need for such high position resolution for the synchroton photons or low energy electrons, since the angle aperture from SR is $\Delta\phi_{SR} \sim 1/\gamma$ and homogenous.

$$R_n A = \frac{R_f A}{(n-1)\frac{G-1}{N-1} + 1} \quad R_n B = \frac{R_f B}{(N-n)\frac{G-1}{N-1} + 1} \quad (4.11)$$

To provide two weighted signals, an extra circuit is added with a charge division style (See Figure 4.12b). This circuit take the 25 signal output from each MPPC and provide two signals A and B , each one depending on the Gain G and the resistance R_n where n is the n-th channel. The equation for proper resistance for N channels are provided in equation 4.11.

The average of A and B provide the total amplitud recorded on the 25 channels while equation 4.12 shows the position of the event ranged from 0 until N .

$$X = \frac{A - B}{A + B} \quad (4.12)$$

4.3. Calibration

For the calibration the LYSO detector was installed on the NA64 detector on RUN I (July 2016). The detector is placed right in front of the ECAL to profit from the

trigger and the beam setup. Since it is the first time the detector is connected to the DAQ[?], a proper gain equalization must be performed. For this purpose, the detector was placed in three different positions refer to the beam as it shows the Figure 4.13. The first configuration (a), allows us to equalized the 25 channels on the X-axis. A beam with pions will hit one crystal lossing its energy by ionisation, which for high particles the minimum ionization is roughly 2 MeV/gcm². Hence the total energy deposition per channels is the width of each crystal (0.4 cm) times the LYSO density (7.1 g/cm³) and the loss energy per density (2 MeV/gcm²) resulting in a 5.68 MeV.

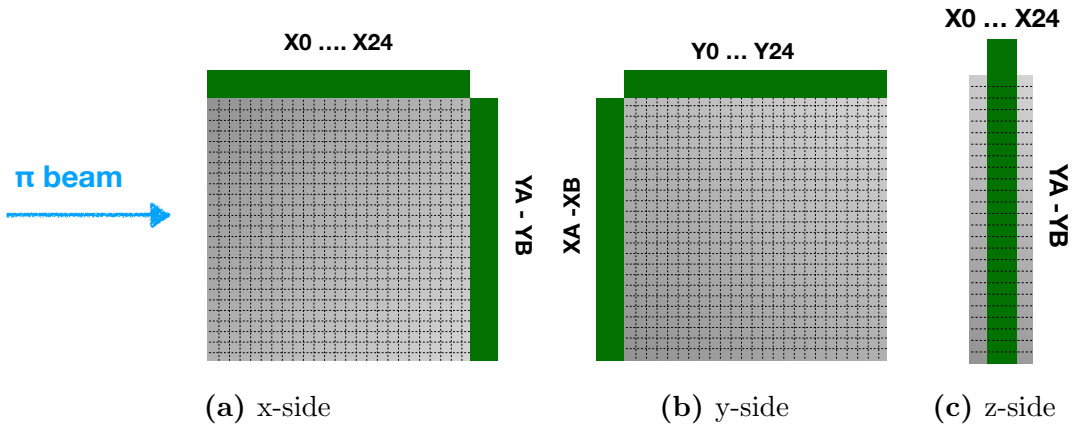


Figure 4.13: Detector position for calibration. Pion beam is always from the left to the right on the three configurations

With a program COOOL designed for monitoring events online (see Figure 4.14), it was possible to look at the histograms were shows the total amplitude register on each channel removing the pedestal. The first spills shows us a Vavilov-Landau distribution on the histograms with a peak value around 20-50 a.u. depending on the channel. Thereafter the bias voltage on the 5 shared channels were adjusted to obtain a considerable same peak value. The range of the voltage for the MPPC goes from 68 V to 72 V therefore, a peak value of around 75 a.u. respect to pedestal was the goal. Once the equalizations is achieved a new run is performed with few spills with enough events to perform the calibration offline.

$$\text{wave}_i = \{a_0, a_1, \dots, a_{30}, a_{31}\} \quad (4.13)$$

The **Run 1459** with 10 spills ($\sim 70k$ events) it is enough to perform the calculations for pedestal position and width. The raw data is a digitized pulse of 32 time samples ??, with one sample each 12 ns thanks to the combination of two ADC's.

$$\text{ped0} = \frac{1}{4} \sum_{i=0,2,4,6} a_i \quad \text{ped1} = \frac{1}{4} \sum_{i=1,3,5,7} a_i \quad (4.14)$$

Two pedestal are calculated from the first 8 time samples according to equation 4.14 from the wave. Afterwards, the pedestal is subtracted from the wave eqn.4.13 according to the position (odd or even)

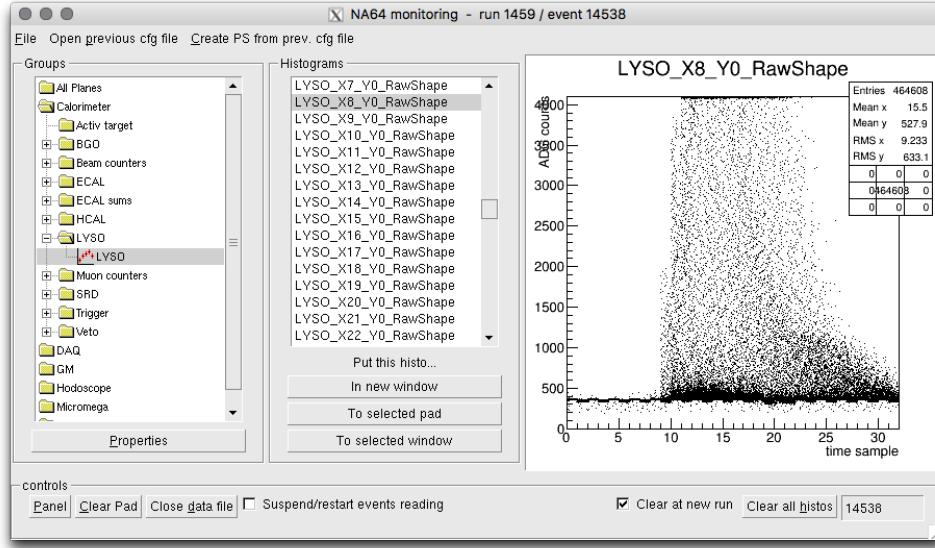


Figure 4.14: Monitoring application COOOL showing a waveform from channel x8. 32 time samples are obtained from the two ADC and 4096 channels for amplitude counts. Pedestal around 400 ADC counts

$$\overline{\text{wave}}_i = \{a_0 - \text{ped0}, a_1 - \text{ped1}, \dots, a_{30} - \text{ped0}, a_{31} - \text{ped1}\} \quad (4.15)$$

For analysis purpose, an estimation of the pedestal signal is performed as the average of ped0 and ped1 . The monitoring program COOOL shows the pedestal while the data taking is running and an example of it is shown in Figure 4.16a. However, a full analysis of the pedestal is performed offline. For each channel an histogram for pedestal is calculated with the average of ped0 and ped1 per triggered event. A Gaussian fit is applied to the pedestal signal and the parameter μ and σ are shown in Figure 4.16b.

A summary of pedestal of each channel on x-axis is presented in Figure 4.16b. The data set represent the μ parameter from a Gaussian distribution, and where $\sigma \sim 1$ for each channel. The graph also shows the average pedestal around 365 for all channels and the RMS of about 25, which highlights the stability of the system and the detector.

The ADC integrates the analog pulse from the detector and then goes to a shaper pulse to deliver the waveform from Figure 4.14. The maximum of this pulse gives the charge integrated from the analog pulse, therefore an histogram with the maximum amplitude will be proportional to the amount of energy deposited by an ionization.

To estimate the energy on the detector, a comparison between the most probable value (MPV) from a Landau fit and the energy loss on a small thickness material is performed. Such way each MPV from each channel can be compared to the 5.68MeV and obtain the calibration factors for each channel. The Figure 4.17 shows an example from this method, where a Landau fit is performed (red line) and it also shows the MIP value (5.68 MeV) is relatively close to the pedestal (a value 0 in the histogram) since the peak expected from SR is around 11MeV. However the separation from the peak value is enough to see the Landau distribution start from 0 counts around 5a.u.

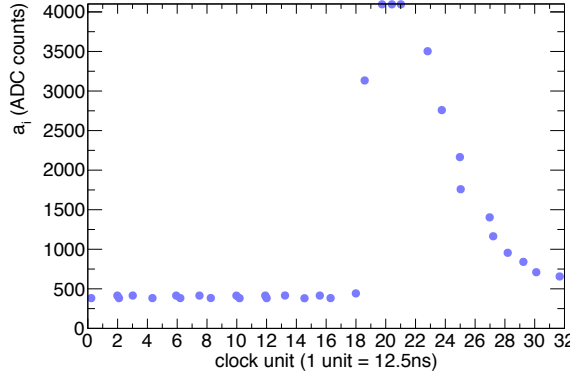


Figure 4.15

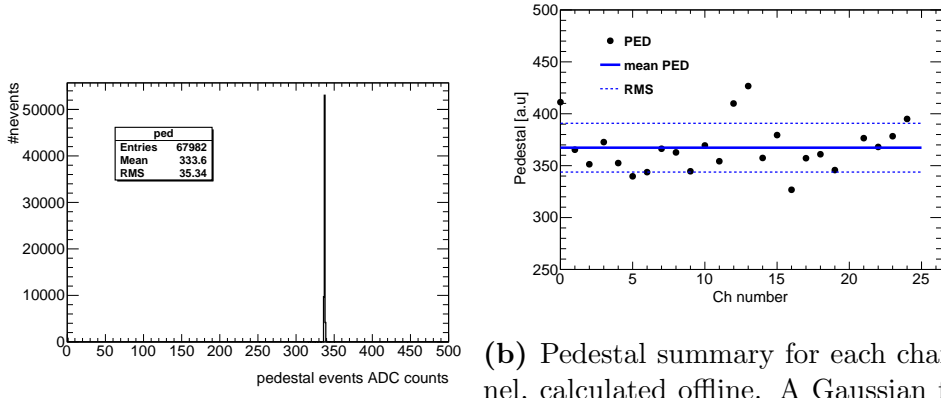


Figure 4.16: Pedestal summary

One set of data (run 1459) was taken with the configuration (a) on Figure 4.13 where a pion beam hits at least one crystal per channel on the x-side. Afterwards the MIP position is identified and estimated the most probable value (MPV) for each channel. A graph who summarize this procedure is shown in Figure 4.18a. Afterwards, the detector is turn over and the electronic boards are swapped to observe each channel on the y-side. Then a 10 spills **run 1463** is recorded and the MIP position is adjusted on each channel to 50a.u. above pedestal. The reason for this number is the maximum ADC count is app 4000 units, and if all the channel provide a signal we will get an overflow on the two weighted signals.

The MIP position for the y-side is shown in Figure 4.18b with an average of 45 a.u.. Both graph shows a MPV=0 para ch number 20, that is because that channel has a high pedestal (~ 3000 ADC counts) and it was remove from all the analysis. The Figure 4.19 shows the pulse from channel 20 which clearly expose a bipolar pulse.

In the configuration (c), when the detector is perpendicular to the beam (Figure 4.13c), the mean energy deposited by a minimum ionizing particle is $E_{\text{mip}} \sim 64\text{MeV}$. It means

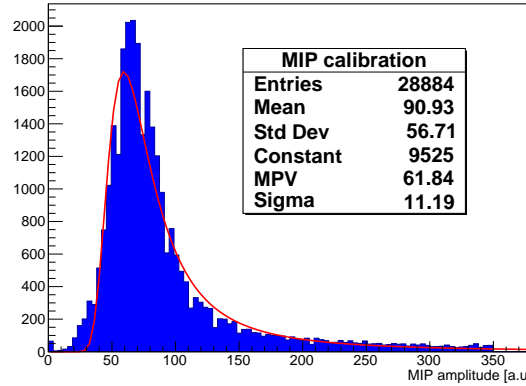


Figure 4.17: Histogram from amplitude when a MIP pass through the crystal across 0.4 cm

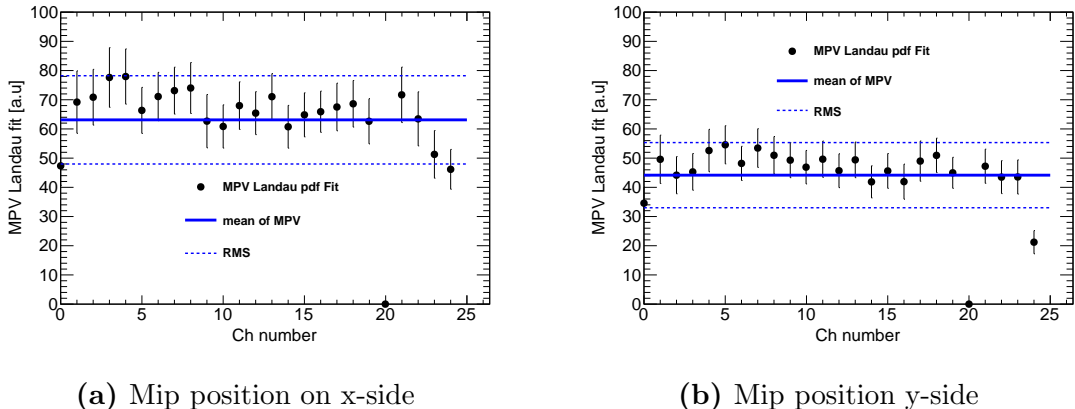


Figure 4.18: Gain equalization. Data sets excluding channel 20 for high pedestal and shape problems.

for every event, the total light collected should be proportional to E_{mip} . The Figure 4.20 correspond to the run 1467, a pion beam, and shows the amount of energy deposited on the LYSO detector. The total amount of energy is calculated as:

$$E = \sum_{ch=0}^{24} a[ch] * c_0[ch] \quad (4.16)$$

where c_0 correspond to the calibration coefficients calculated as $c_0[ch] = 5.68/\text{MPV}[ch]$ and $a[ch]$ correspond to the max amplitude per ch on each event.

A Landau fit is applied to total energy deposited on x-side, and a 66MeV as MPV is obtained compare to the 64MeV expected. To estimate the energy resolution, the parameter ξ from a Landau pdf is used as sigma and the resolution is estimated by full width at half maximum (FWHM) where the maximum correspond to the MPV on the Landau pdf.

$$\text{FWHM} = 2.355\sigma \quad (4.17)$$

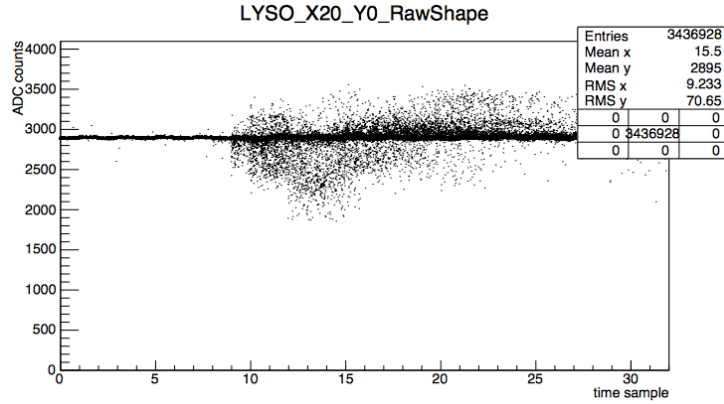


Figure 4.19: Bad channel

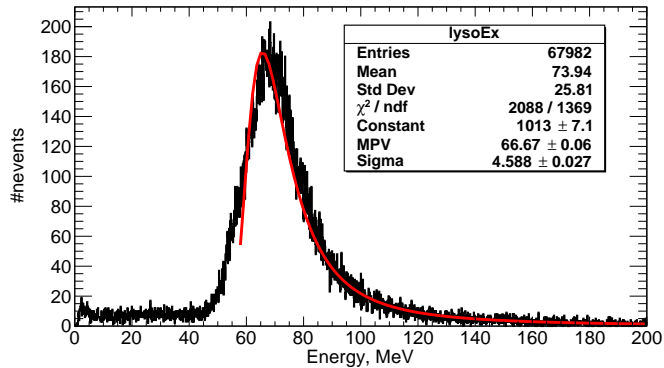


Figure 4.20: Sum of every channel amplitude with the calibration coefficient provided in ref

Where for the x-side gives a Resolution of : $2.355 * 4.588 / 66.67 = 16\%$, early reported on ?? a 8% of energy resolution of one crystal at 662keV.

On the y-side, every channel was equalized to around the same MPV value (50 ADC counts). Therefore, both weighted signal should show the same distribution with slightly same MPV values. The Figure 4.21 shows a Landau pdf for each weighted signal Y_A and Y_B since both are the sum over all channels with some gain factors.

Applying a Landau fit over the sum of both Y_A and Y_B amplitudes, we can estimate the resolution for the y-axis. The Figure 4.22 shows the histogram of both weighted signal with a Landau fit. With a MPV of 1207 (ADC counts) and a $\xi = 89.5$ results in a 17% energy resolution at 64MeV.

The charge division circuit was made to obtain the position of the particles crossing the detector along y-side. The position is obtained according to equation 4.12. On the other hand, to calculate the position on the x-side, a different treatment must be done. Using a simple center of mass calculation for each x channel the position can be estimated like:

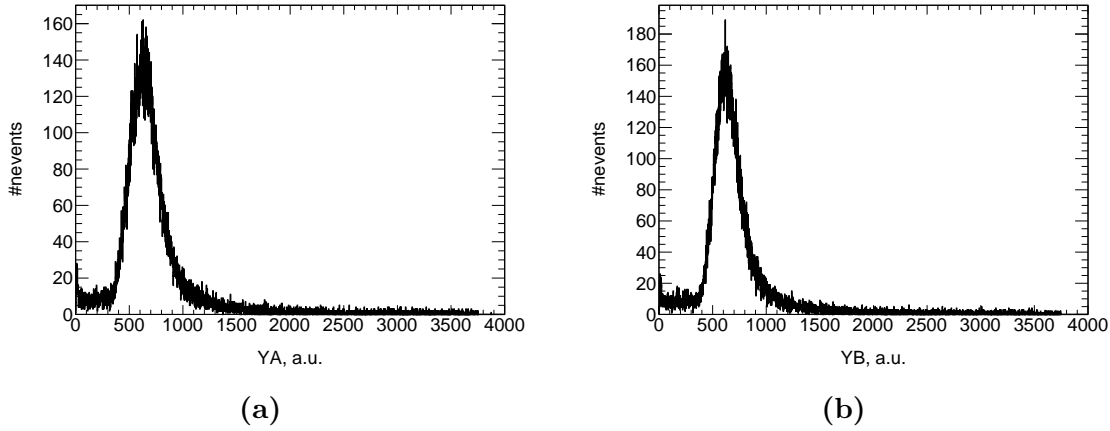


Figure 4.21: Weighted signal amplitude distribution on run 1463 (pion beam).

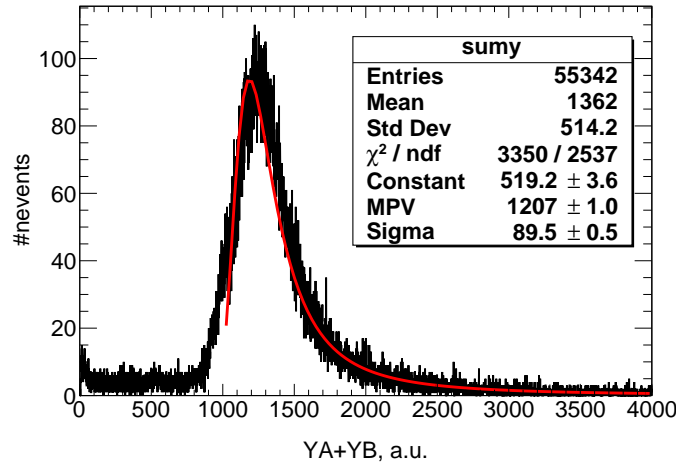


Figure 4.22

$$X_{\text{pos}} = \frac{\sum_{x=0}^{24} E[x] * x}{\sum_{x=0}^{24} E[x]} \quad (4.18)$$

where x represent the channel number and $E[x]$ the energy deposited on that channel. The Figure 4.24 shows the position distribution of the beam for each triggered event. About 6 columns of crystals (strips) are fired, while in y-side 9 strips are fired resulting in a beam size of $2.4 \times 3.6 \text{cm}^2$.

To ensure the quality of the equalization two set of runs were taken with pion beam. Where the results for Run 1467 are present in the previous figure. The Run 1468 differ from the previous one by the beam position. The moving table were the LYSO detector is placed was moved by 3 centimeters. So it could be possible to figure out what are the small events present in the x position graph 4.24a presented from centimeter 2 to 5.

The gaussian like distribution on the first 5 centimeters remain after move the beam and represent a change in the pedestal on these channels for this particulars runs.

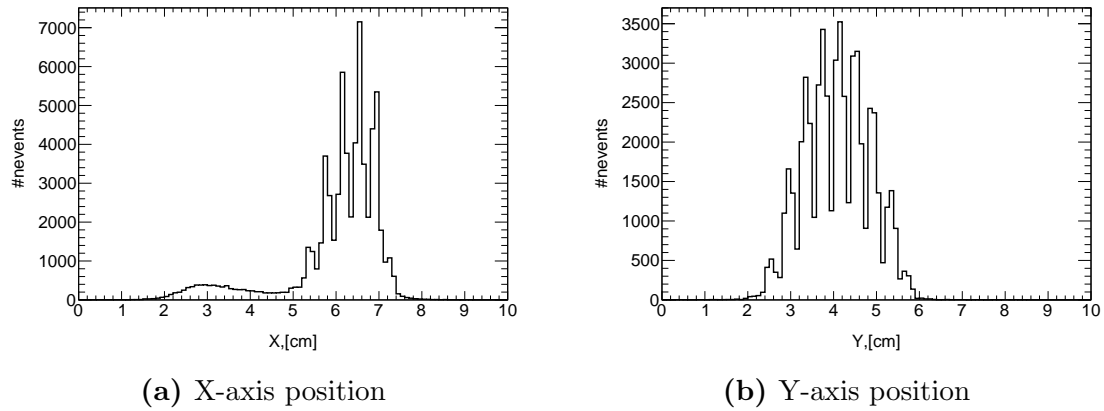


Figure 4.23: Position reconstructed by x and y side using center of mass for X-axis and the equation 4.12 for Y-axis.

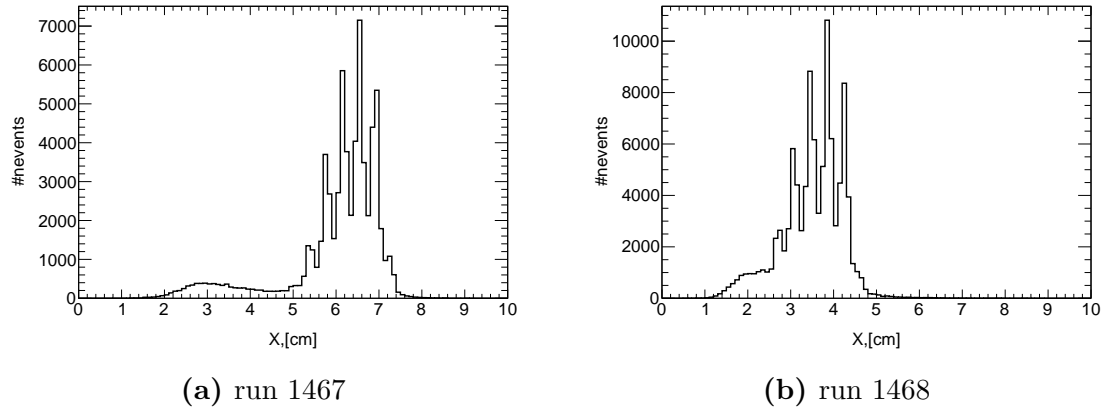


Figure 4.24: X position comparison from Run 1467 y 1468.

Using both distribution, x and y position is possible to obtain a 2D profile of the pion beam on the detector. This profile highlight the crystal matrix present in the detector.

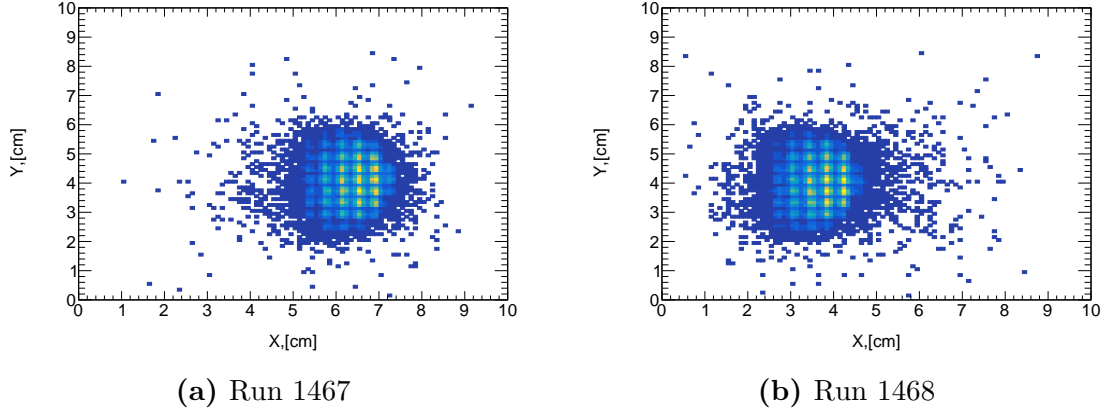


Figure 4.25: Beam profile for two different pion runs, with different x position.

4.4. Time resolution

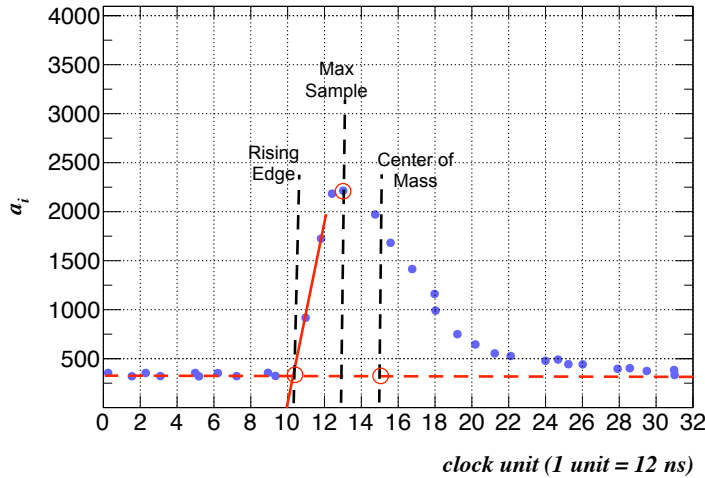


Figure 4.26: Timing methods on wave sample

In order to estimate the timing for each detector, the time reference is the first counter upstream. According to the setup shown in Figure 4.6, the first counter is the scintillator $S1$.

To calculate the timing from the 32 time samples, three methods were applied.

Max sample

From the 32 time samples, the max amplitude is recorded and the time sample when this happened is set as the time t_0 . This method is very sensitive to saturation of the ADC range. The scintillators reach easily the maximum ADC counts, and then timing will be independent of the max amplitude reached by the detector.

The Figure ?? shows the t_0 distribution calculated with this method. The majority of the events the counter $S1$ saturate the ADC, therefore, two sharp peaks are present at

237ns(12,5*19) and 250ns(12,5*20). Separated exactly 12,5 ns shows that the counter is saturated at the same time sample, either in one ADC or in the next one.

Center of Mass

This method estimate the center of mass of each pulse, and the result represent t_0 . The center of mass for one pulse is calculated as :

$$t_0 = \frac{\sum_{i=8}^{31} a_i * i}{\sum a_i} \quad (4.19)$$

which consider the amplitudes a_i after the time samples for pedestal estimation. Only the time samples after 8 are considered.

Rising Edge

The last method calculate the intersection of the rising edge with the time axis to get the origin time (t_0). Again using the maximum of amplitud, the algorithym look for the time sample with half of the maximum or above and return the index of the time sample. Afterwards, from the time sample with half of the maximum (a_j) and the previous one a_{j-1} is possible to obtain the intersection of this linear with the axis time.

$$t_0 = t_j - \frac{a_j}{a_j - a_{j-1}} \quad (4.20)$$

This method present the advantage of being non-sensitive to saturation, because of the use of two time samples before the saturation occurs and in the worst case when there is no time sample between the base line and the saturated maximum the origin time will be the time sample before the saturation.

Time is defined respect to the first counter S1, and calculated with constant fraction method where:....

The temporal resolution on a single channel is shown in ..

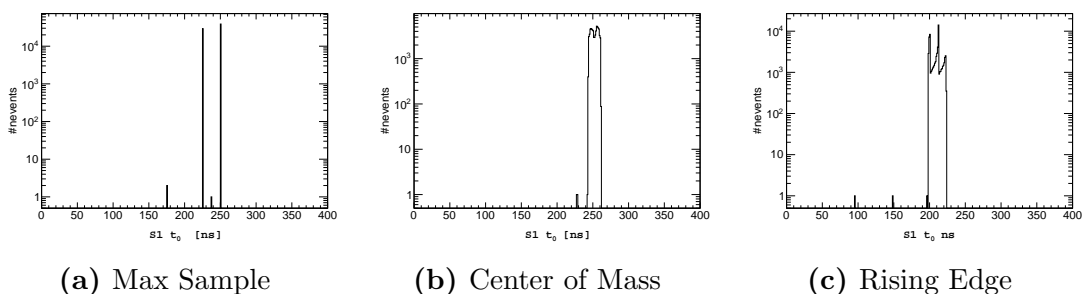


Figure 4.27: Timing calculated for S1 with three different methods; Max sample, Center of Mass and Rising Edge.

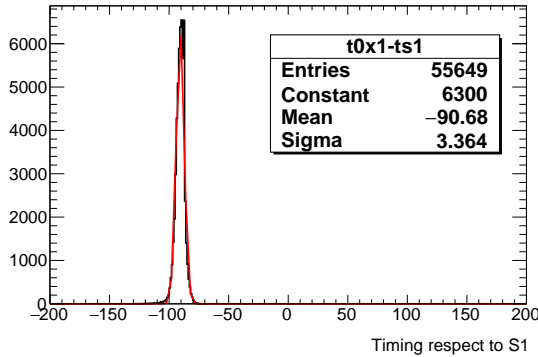


Figure 4.28

4.5. Hadron rejection

During the July Run for the NA64 experiment, a set of runs with the LYSO detector as SRD were taken. With an average beam intensity of $7.5 \cdot 10^5$ events/s registered on S0, these runs are considered low intensity. For tagging the electrons and reject the hadrons, it is important to know their signature on LYSO. For this purpose, we can exploit two features of the array of crystals.

Each signal from the x-axis, correspond to the amount of light produce by the column of crystals in certain x position. All the SR produced by the electron beam in the region of the LYSO detector is collected by 25 columns. Therefore, we should expect a homogeneous distribution of light in these 25 channels. To calculate the amount of hadrons present in each spill or in the total triggered events, we use the electron (ECAL) and hadron (HCAL) calorimeters to provide the identification for our analysis.

4.5.1. BGO hadron suppression

The crystal were calibrated by comparing the peak position from the energy deposited by minimum ionizing particles with the one from Monte Carlo simulation, which corresponds about 64MeV.

The next two sections show the two equivalent approach for this detector, to calculate the level of hadron suppression factor.

4.5.2. Total energy

In the Section 4.2.3, the level of hadron suppression is calculated using the total energy deposited as threshold.

4.5.3. Strips triggered

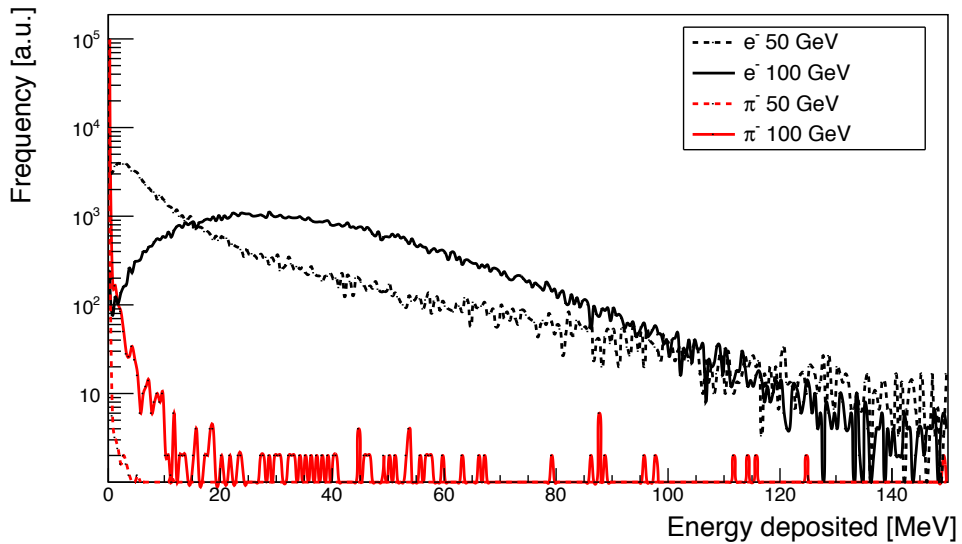


Figure 4.29: Results of the GEANT4 simulation for the energy detected by BGO for 50/100 GeV e^- (black dashed/solid line) and 50/100 GeV π^- (red dashed/solid line).

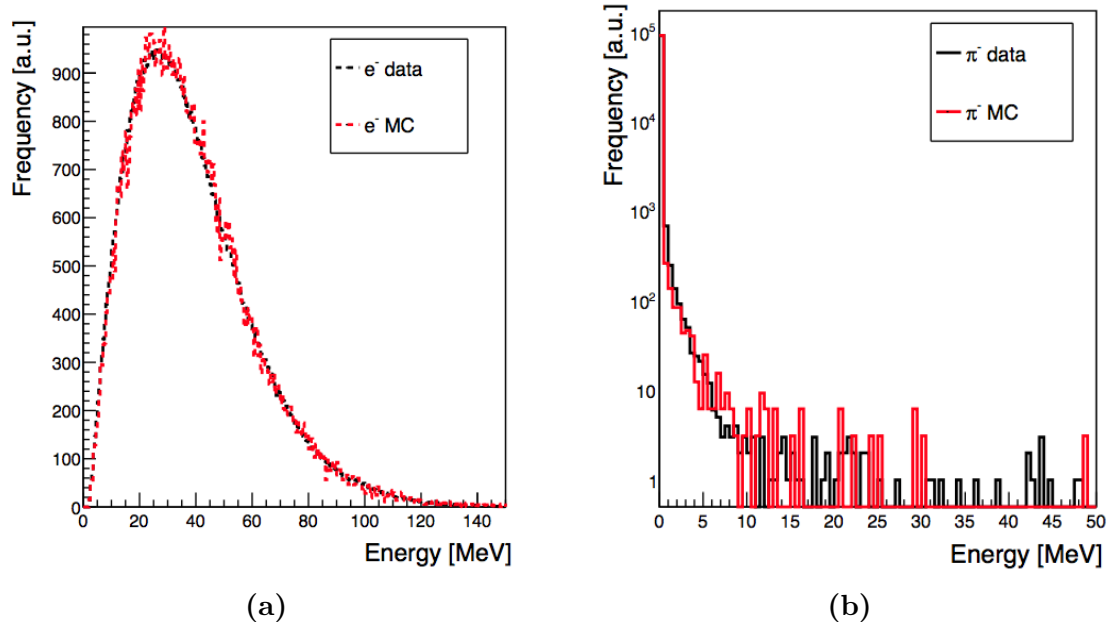


Figure 4.30

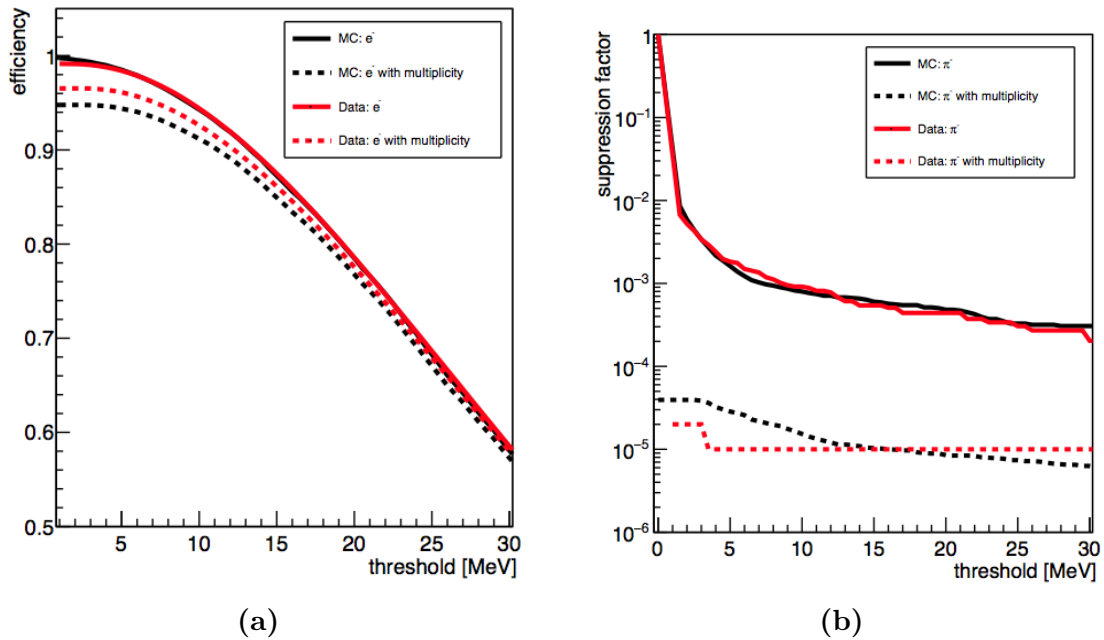


Figure 4.31

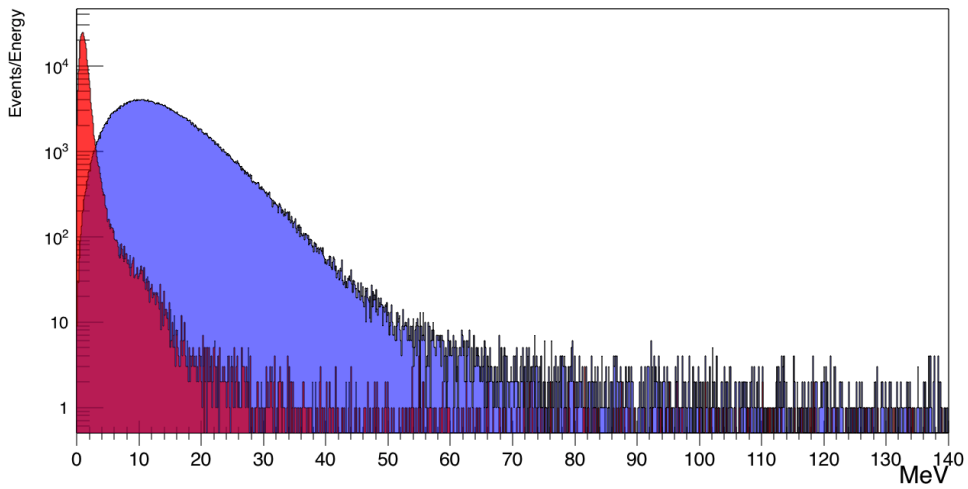


Figure 4.32: Energy deposition of Synchrotron Radiation configuration. Electrons tagged from S_{e^-} in blue and hadrons S_H in red.

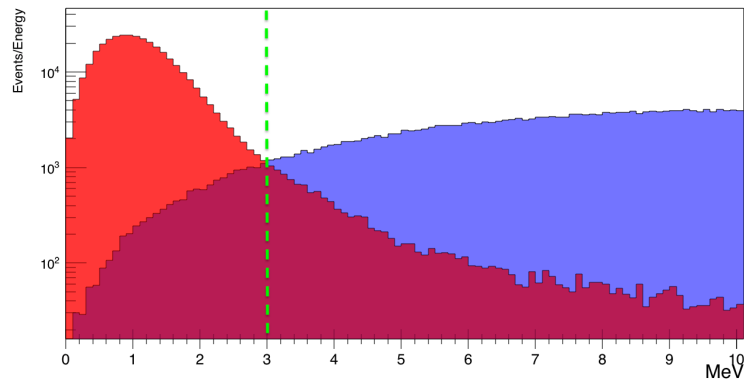


Figure 4.33

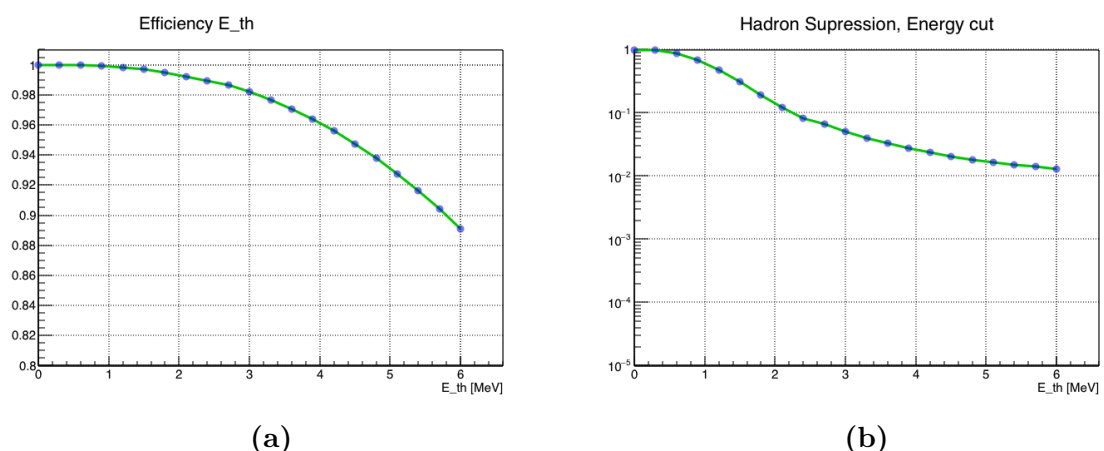


Figure 4.34

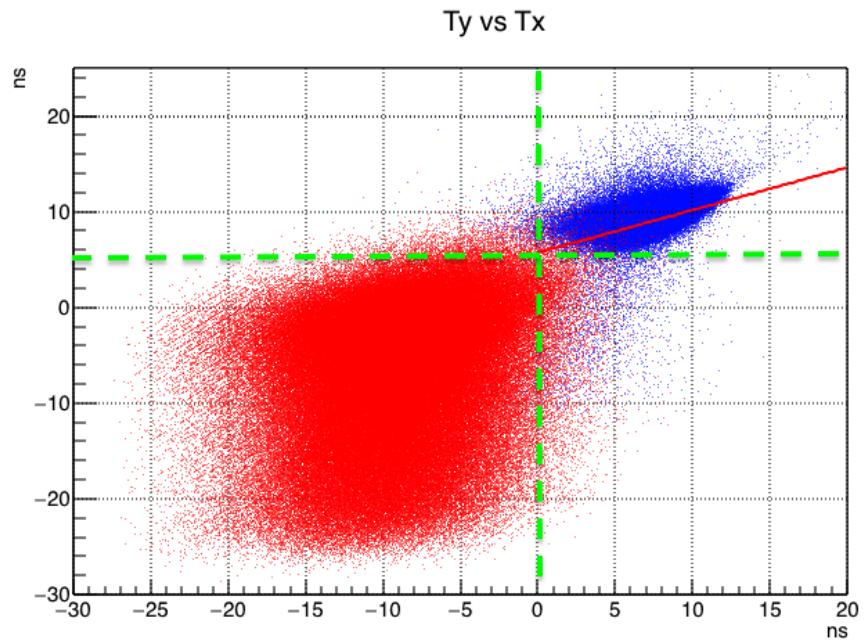


Figure 4.35

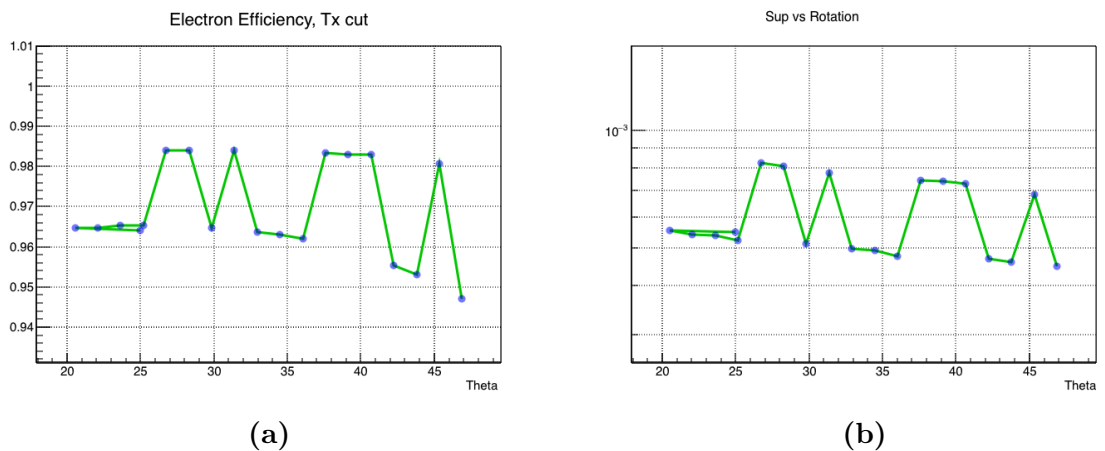


Figure 4.36

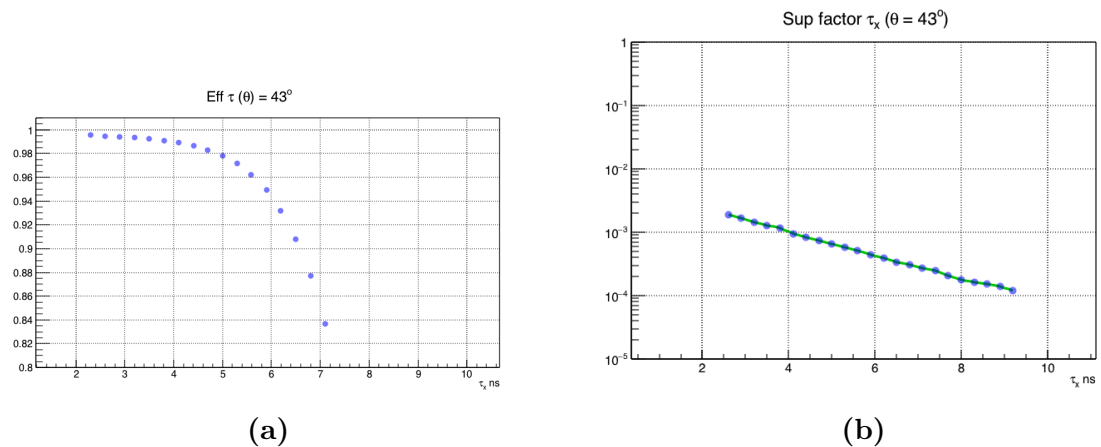


Figure 4.37

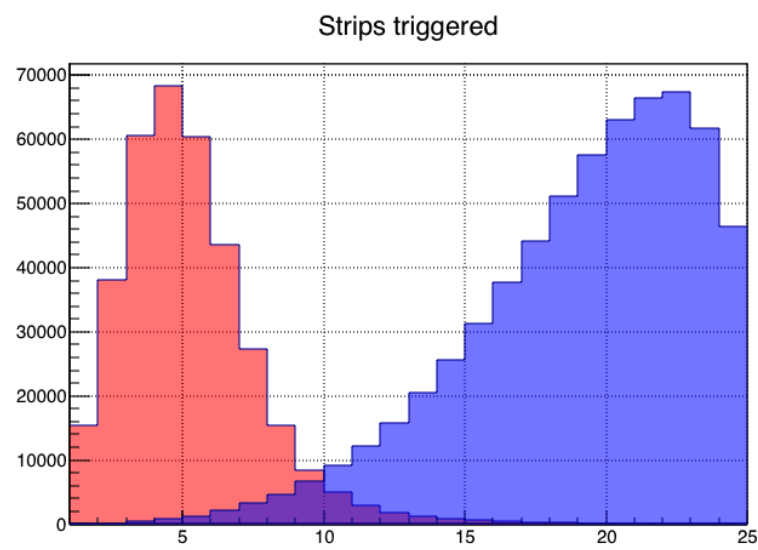


Figure 4.38

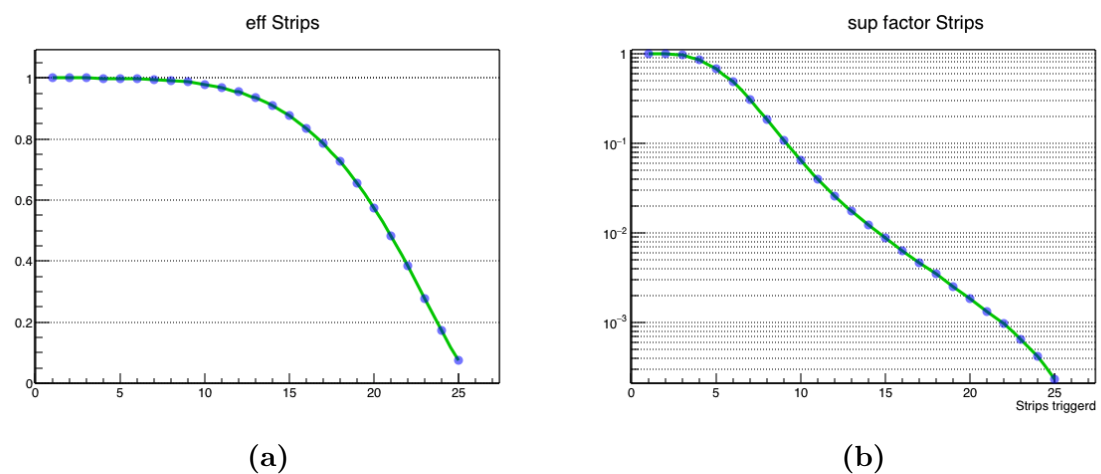


Figure 4.39

4.6. Experimental Results

4.7. Summary

5. Conclusion

A. Appendix

- A.1. Mechanical Measurements sTGC Module 0
- A.2. PMT RT7525 Data Sheet
- A.3. NA64 Experiment:Data structure
- A.4. NA64 Experiemnt:DAQ system

Bibliography

- [1] ATLAS collaboration, “*Observation of a new particle in the search for the Standard Model Higgs boson with the ATLAS detector at the LHC*”, Physics Letters B **716** (2012) 1–29.
- [2] CMS collaboration, “*Observation of a new boson at a mass of 125 GeV with the CMS experiment at the LHC*”, Physics Letters B **716** (2012) 30–61.
- [3] G.Mikenberg et al., *Thin-gas gap chambers for hadronic calorimetry*, Nucl. Instr. and Meth. A **265** (1988) 223–227.
- [4] The LEP Collaboration, *Precision Electroweak Measurements on the Z Resonance*, Phys. Rep. **427** (2006) 257–454.
- [5] V.Smakhtin et al., *Thin Gap Chamber upgrade for SLHC: Position resolution in a test beam*, Nucl. Instr. and Meth. A **598** (2009) 196–200.
- [6] S.Majeski, *A Thin wire chamber operating in a high multiplication mode*, Nucl. Instr. and Meth A **217** (1983) 265–271.
- [7] W. Blum, *Particle Detection with Drift Chambers*. Springer, 2008.
- [8] Garfield++, *Project web page*, <http://garfieldpp.web.cern.ch/garfieldpp/>.
- [9] R. Veenhof, *GARFIELD, recent developments*, Nucl. Instr. and Meth. A **419** (1988) 726–730.
- [10] F.Sauli, *Principle of operation of multiwires proportional and drift chambers*. CERN, 1977.
- [11] *sTGC construction’s manual*, <https://edms.cern.ch/document/1399978/1>.
- [12] *Mini-X Gun Datasheet*, <http://www.amptek.com/pdf/minix.pdf>.
- [13] GIF++, *The new Gamma Irradiation Facility*, <https://espace.cern.ch/sba-workspace/gifpp/>.
- [14] O.Sasaki et al., *ASD IC for the thin gap chambers in the LHC ATLAS Experiment*, IEEE Transactions on Nuclear Science **46** (1999) 1861–1864.

- [15] A. Abusleme et al., *Performance of a full-size small-strip thin gap chamber prototype for the ATLAS new small wheel muon upgrade*, Nucl. Instr. and Meth. A **817** (2016) 85–92.
- [16] NA64 Experiment, *Search for dark sectors in missing energy events*, <https://na64.web.cern.ch>.
- [17] D. Banerjee et al. [NA64 Collaboration], *Search for Invisible Decays of Sub-GeV Dark Photons in Missing-Energy Events at CERN SPS*, Physical Review Letters **118** (2017) 011802.
- [18] A. Andreas et al., *Proposal for an Experiment to Search for Light Dark Matter at the SPS*, CERN-SPSC-2013-034 **SPSC-P-348** (2013) 011802, arXiv:1312.3309.
- [19] *SPS beam lines*, <http://cern.ch/sba>.
- [20] D. Banerjee, P. Crivelli and A. Rubbia, *Beam Purity for Light Dark Matter Search in Beam Dump Experiments*, Adv. High Energy Phys. **105730** (2015) .
- [21] W. Busza, M. Chen and D. Luckey, *Application of synchrotron radiation for the identification of electrons in high energy beams*, Nucl. Instr. and Meth. **105** (1972) 613.
- [22] J. S. Dworkin et al, *Electron identification using a synchrotron radiation detector*, Nucl. Instr. and Meth. A **247** (1986) 412.
- [23] R. Cryttenden, *Synchrotron radiation detector for tagging electrons*, Nucl. Instr. and Meth. A **276** (1989) 643–646.
- [24] H. Wiedemann, *Particle Accelerator Physics*. Springer, 2007.
- [25] S. Gobain, *BGO Bismuth Germanate*, <http://www.crystals.saint-gobain.com/products/bgo>.
- [26] S. Gobain, *Prelude 420 LYSO*, <http://www.crystals.saint-gobain.com/products/prelude-420-LYSO>.
- [27] O. Soto et al., *Characterization of novel Hamamatsu Multi Pixel Photon Counter (MPPC) arrays for the GlueX experiment*, Nucl. Instr. and Meth. A **739** (2014) 89–97.